CGC/saturation approach for high energy soft interactions: 'soft' Pomeron structure and v_n in hadron and nucleus collisions from Bose-Einstein correlations

E. Gotsman,[1,*] E. Levin,[1,2,†] and U. Maor[1,‡]

[1] *Department of Particle Physics, School of Physics and Astronomy, Raymond and Beverly Sackler Faculty of Exact Science, Tel Aviv University, Tel Aviv, 69978, Israel*
[2] *Departemento de Física, Universidad Técnica Federico Santa María, and Centro Científico-Tecnológico de Valparaíso, Avda. Espana 1680, Casilla 110-V, Valparaíso, Chile*

(Dated: July 25, 2016)

In the framework of our model of soft interactions at high energy based on CGC/saturation approach, we show that Bose-Einstein correlations of identical gluons lead to large values of v_n. We demonstrate how three dimensional scales of high energy interactions: hadron radius, typical size of the wave function in diffractive production of small masses (size of the constituent quark), and the saturation momentum, influence the values of BE correlations, and in particular, the values of v_n. Our calculation shows that the structure of the 'dressed' Pomeron leads to values of v_n which are close to experimental values for proton-proton scattering, 20% smaller than the observed values for proton-lead collisions, and close to lead-lead collisions for 0-10% centrality. Bearing this result in mind, we conclude that it is premature to consider, that the appearance of long range rapidity azimuthal correlations are due only to the hydrodynamical behaviour of the quark-gluon plasma.

PACS numbers: 12.38.-t,24.85.+p,25.75.-q

arXiv:1607.00594v3 [hep-ph] 22 Jul 2016

I. INTRODUCTION

In our previous paper[1] we showed that Bose-Einstein correlations lead to strong azimuthal angle correlations, which do not depend on the difference in rapidity of the two produced hadrons (long range rapidity LRR correlations). The mechanism suggested by us, has a general origin, and thus manifests itself in hadron-hadron, hadron-nucleus and nucleus-nucleus interactions, and generates the correlation that has been observed experimentally [2–12]. The fact that Bose-Einstein correlations lead to strong LRR azimuthal angle correlations, was found long ago in the framework of Gribov Pomeron calculus[13], and it has been re-discovered recently in Refs.[14, 15] in CGC/saturation approach[16]. In Ref.[1] it was noticed, that these correlations give rise to v_n for odd and even n, while all other mechanisms in CGC/saturation approach, including the correlations observed in [14, 15], generate only v_n with even n.

The LRR correlations in CGC/saturation approach originate from the production of two parton showers (see Fig. 1). The double inclusive cross section is described by the Mueller diagram of Fig. 1-b, in which the production of gluons from the parton cascade, is described by the exchange of the BFKL Pomeron (wavy double line in Fig. 1-b), while, due to our poor theoretical knowledge of the confinement of quarks and gluons, the upper and lower blobs in Fig. 1-b require modeling. .

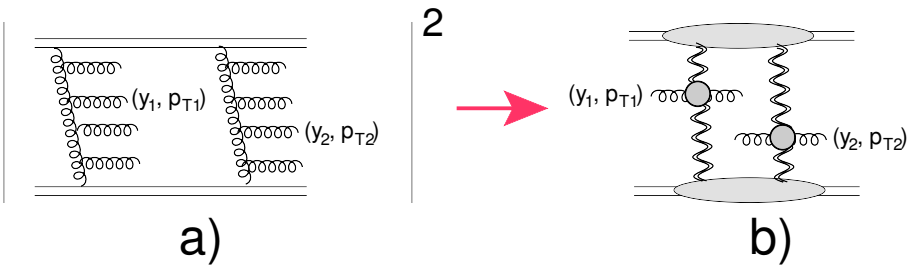

FIG. 1: Production of two gluons with $(y_1, \boldsymbol{p}_{T1})$ and $(y_2, \boldsymbol{p}_{T2})$ in two parton showers (Fig. 1-a). Fig. 1-b shows the double inclusive cross section in the Mueller diagram technique [19]. The wavy lines denote the BFKL Pomerons[20, 21].

If the two produced gluons have the same quantum numbers, one can see that in addition to the Mueller diagram for different gluons (see Fig. 1-b), we need to take into account a second Mueller diagram of Fig. 2-b, in which two gluons with $(y_1, \boldsymbol{p}_{T2})$ and $(y_2, \boldsymbol{p}_{T1})$ are produced. When $\boldsymbol{p}_{T1} \to \boldsymbol{p}_{T2}$, the two production processes become identical, leading to the cross section σ (two identical gluons) $= 2\sigma$ (two different gluons), as one expects. When $|\boldsymbol{p}_{T2} - \boldsymbol{p}_{T1}| \gg 1/R$, where R is the size of the emitter[17], the interference diagram becomes small and can be neglected.

The angular correlation emanates from the diagram of Fig. 2-b, in which the upper BFKL Pomerons carry momentum $\boldsymbol{k} - \boldsymbol{p}_{T,12}$ with $\boldsymbol{p}_{T,12} = \boldsymbol{p}_{T1} - \boldsymbol{p}_{T2}$, while the lower BFKL Pomerons have momenta $\boldsymbol{k}$. The Mueller diagrams for the correlation between two gluons are shown in Fig. 2.

After integration over k_T, the sum of diagrams Fig. 2-a and Fig. 2-b can be written as

$$\frac{d^2\sigma}{dy_1\, dy_2 d^2p_{T1} d^2p_{T2}}\,(\text{identical gluons}) \;=\; \frac{d^2\sigma}{dy_1\, dy_2 d^2p_{T1} d^2p_{T2}}\,(\text{different gluons})\,\Big(1 \,+\, C\left(R|\boldsymbol{p}_{T2} - \boldsymbol{p}_{T1}|\right)\Big) \tag{1}$$

Eq. (1) coincides with the general formula for the Bose-Einstein correlations [17, 18]

$$\frac{d^2\sigma}{dy_1\, dy_2 d^2p_{T1} d^2p_{T2}}\,(\text{identical gluons}) \;\propto\; \Big\langle 1 \,+\, e^{ir_\mu Q_\mu}\Big\rangle \tag{2}$$

where averaging $\langle \dots \rangle$ includes the integration over $r_\mu = r_{1,\mu} - r_{2,\mu}$. There is only one difference: $Q_\mu = p_{1.\mu} - p_{2,\mu}$ degenerates to $\boldsymbol{Q} \equiv \boldsymbol{p}_{T,12}$, due to the fact that the production of two gluons from the two parton showers do not depend on rapidities. Note, that the contribution of Fig. 2-b does not depend on the rapidity difference $y_1 - y_2$ nor on y_1 and y_2. For $y_1 = y_2$ Eq. (1) follows directly from the general Eq. (2), and the interference diagram of Fig. 3-b leads to Eq. (1), and allows us to calculate the typical correlation radius and the correlation function $C\left(R|\boldsymbol{p}_{T2} - \boldsymbol{p}_{T1}|\right)$. On the other hand, for $y_1 \neq y_2$ but for $\boldsymbol{p}_{T1} = \boldsymbol{p}_{T,2}$ Eq. (1), gives a constant which does not depend on y_1 and y_2. However, in general case $y_1 \neq y_2$ and $\boldsymbol{p}_{T1} \neq \boldsymbol{p}_{T,2}$ the diagram of Fig. 2-b looks problematic [1], since it seems to describe the interference between two different final states. In appendix A we demonstrate that the contribution of Fig. 2-b does not vanish even in this general case. Note, that for $y_1 = y_2$, the sum of two Mueller diagrams , indeed, relates to the interference between two diagrams, as is shown in Fig. 3-a and Fig. 3-b. For these kinematics, as we have mentioned

$$C\left(R|\boldsymbol{p}_{T2} - \boldsymbol{p}_{T1}|\right) \;=\; \Big\langle e^{i\boldsymbol{r}_T\cdot\boldsymbol{Q}_T}\Big\rangle \qquad \text{where} \qquad \boldsymbol{Q}_T \,=\, \boldsymbol{p}_{T,12} \tag{3}$$

For $\boldsymbol{p}_{T1} = \boldsymbol{p}_{T2}$, the sum of two Mueller diagrams can also be viewed as the interference of two diagrams of Fig. 3-c and Fig. 3-d, leading to

$$C\left(|0|\right) \;=\; \Big\langle e^{i\boldsymbol{r}^+\boldsymbol{Q}_- + i\boldsymbol{r}^-\boldsymbol{Q}_+}\Big\rangle \tag{4}$$

The calculation of the Mueller diagram shows that this average does not depend on y_1 and y_2.

Remembering that for two parton showers in each order of perturbative QCD, (or in other words at fixed multiplicity of the produced gluons) the amplitude can be written in the factorized form $A = A_L\left(r_+, r_-\right)\, A_T\left(\boldsymbol{r}_T\right)$ leading to

$$\Big\langle e^{ir_\mu\, Q_\mu}\Big\rangle \;=\; \underbrace{\Big\langle e^{i\boldsymbol{r}_T\cdot\boldsymbol{Q}_T}\Big\rangle}_{\text{averaging over } r_T} \times \underbrace{\Big\langle e^{i\boldsymbol{r}^+\boldsymbol{Q}_- + i\boldsymbol{r}^-\boldsymbol{Q}_+}\Big\rangle}_{\text{averaging over } r_+, r_-} \tag{5}$$

In our opinion, the above discussion shows that the Mueller diagram of Fig. 2-b, does not characterize the interference between two orthogonal states, but is an economical way to describe the independence of identical gluon production on rapidities, providing the smooth analytical description of the cross section from $y_1 = y_2$ to the general case $y_1 \neq y_2$. Since this point is not obvious we would like to recall the main features of the leading log(1/x) approximation (LLA). In the LLA we account for the following kinematic region[20, 21] for the production of two parton showers (see Fig. 4):

$$\begin{array}{rcl}
\text{first parton shower} & \to & Y > \dots > y_i > \dots > y_{n_1} > y_1 > y_{n_2} > \dots > y_i > \dots > 0; \\
\text{second parton shower} & \to & Y > \dots > y_i > \dots > y_{n_3} > y_2 > y_{n_4} > \dots > y_i > \dots > 0; \\
\text{parameters of LLA}: \;\bar{\alpha}_S \ll 1 & & \bar{\alpha}_S\left(y_{i+1} - y_i\right) \geq 1;\;\; \bar{\alpha}_S\left(Y - y_i\right) \geq 1;\;\; \bar{\alpha}_S\left(y_i - 0\right) \geq 1;\;\; \bar{\alpha}_S\left(Y - y_1\right) \geq 1; \\
& & \bar{\alpha}_S\left(Y - y_2\right) \geq 1; \bar{\alpha}_S\left(y_1 - 0\right) \geq 1;\;\; \bar{\alpha}_S\left(y_2 - 0\right) \geq 1;\;\; \bar{\alpha}_S\left(y_1 - y_2\right) \geq 1;
\end{array} \tag{6}$$

The cross sections of double inclusive productions can be calculated in LLA for the production of two parton showers

---

[1] We thank Alex Kovner for vigorous discussions on this subject.

in the following way:

$$
\begin{aligned}
\frac{d^2\sigma^{\text{different gluons}}}{dy_1\,dy_2 d^2p_{T1}d^2p_{T2}} &= \sum_{n_1+n_2-2>2}^{\infty}\ \sum_{n_3+n_4-2>2}^{\infty}\int d\Phi^{(1)}_{n_1+n_2}d\Phi^{(2)}_{n_3+n_4}\,|A^{\text{different gluons}}\left(\{y_i,p_{Ti}\};y_1,p_{T1};y_2,p_{T2}\right)|^2 \\
&= \sum_{n_1+n_2=n-2>2}^{\infty}\ \prod_{Y>y_i>y_1}^{n_1}\int_{y_{i-1}}^{y_{i+1}}dy_i d^2p_{T,i}\ \prod_{y_1>y_i>0}^{n_2}\int_{y_{i-1}}^{y_{i+1}}dy_i d^2p_{T,i} \qquad (7a)\\
&\times \sum_{n_3+n_4=n'-2>2}^{\infty}\ \prod_{Y>y_i>y_2}^{n_3}\int_{y_{i-1}}^{y_{i+1}}dy_i d^2p_{T,i}\ \prod_{y_2>y_i>0}^{n_4}\int_{y_{i-1}}^{y_{i+1}}dy_i d^2p_{T,i} \\
&\times \left|\Gamma^2 A_{n_1n_2}\left(2\to n|\{y_i,p_{Ti}\};y_1,\boldsymbol{p}_{T1}\right)A_{n_3n_4}\left(2\to n|\{y_i,p_{Ti}\};y_2,\boldsymbol{p}_{T2}\right)\right|^2 \\
&\xrightarrow{\text{LLA}} \sum_{n_1+n_2=n-2>2}^{\infty}\ \prod_{Y>y_i>y_1}^{n_1}\int_{y_{i-1}}^{y_{i+1}}dy_i d^2p_{T,i}\ \prod_{y_1>y_i>0}^{n_2}\int_{y_{i-1}}^{y_{i+1}}dy_i d^2p_{T,i} \qquad (7b)\\
&\times \sum_{n_3+n_4=n'-2>2}^{\infty}\ \prod_{Y>y_i>y_2}^{n_3}\int_{y_{i-1}}^{y_{i+1}}dy_i d^2p_{T,i}\ \prod_{y_2>y_i>0}^{n_4}\int_{y_{i-1}}^{y_{i+1}}dy_i d^2p_{T,i} \\
&\times \left|\Gamma^2 A_{n_1n_2}\left(2\to n|\{y_i=0,p_{Ti}\};y_1=0,\boldsymbol{p}_{T1}\right)A_{n_3n_4}\left(2\to n|\{y_i=0,p_{Ti}\};y_2=0,\boldsymbol{p}_{T2}\right)\right|^2
\end{aligned}
$$

where $d\Phi^{(1)}_{n_1+n_2}$ and $d\Phi^{(2)}_{n_3+n_4}$ are the phase spaces of the produced gluons in the first and second parton showers. $A^{\text{different gluons}}\left(\{y_i,p_{Ti}\};y_1,p_{T1};y_2,p_{T2}\right)=\Gamma^2 A_{n_1n_2}\left(2\to n|\{y_i,p_{Ti}\};y_1,\boldsymbol{p}_{T1}\right)A_{n_3n_4}\left(2\to n|\{y_i,p_{Ti}\};y_2,\boldsymbol{p}_{T2}\right)$ (see Fig. 4) and all other notations are shown in Fig. 4.

The transition from Eq. (7a) to Eq. (7b), occurs due to the fact that we want to obtain the log contribution $\propto (y_{i+1}-y_{i-1})$ for each dy_i, These logarithms stem from the integration of the phase space of produced particles, while we can neglect the y_i dependence of the production amplitude. In other words, the production amplitudes are functions *only* of the transverse momenta and Eq. (7b) shows that the longitudinal degrees of freedom can be factorize out [20, 21].

Eq. (7a) after integrations over y_i, can be re-written in a more efficacious form , viz.

$$
\begin{aligned}
\frac{d^2\sigma}{dy_1\,dy_2 d^2p_{T1}d^2p_{T2}} &= \sum_{n_1+n_2=n-2>2}^{\infty}\ \sum_{n_1+n_2=n'-2>2}^{\infty}\underbrace{\frac{1}{n_1!}\left(Y-y_1\right)^{n_1}\ \frac{1}{n_2!}\left(y_1-0\right)^{n_2}\ \frac{1}{n_3!}\left(Y-y_2\right)^{n_3}\ \frac{1}{n_4!}\left(y_2-0\right)^{n_4}}_{\text{integral over the longitudinal phase space}} \qquad (8)\\
&\times \int\prod_i d^2p_{Ti}\,|\Gamma^2 A_{n_1n_2}\left(2\to n|\{y_i=0,p_{Ti}\};y_1=0,\boldsymbol{p}_{T1}\right)A_{n_3n_4}\left(2\to n|\{y_i=0,p_{Ti}\};y_2=0,\boldsymbol{p}_{T2}\right)|^2
\end{aligned}
$$

Summing over n_i we obtain the Mueller diagram of Fig. 1.

For identical particles we need to replace

$$
\begin{aligned}
&A^{\text{different gluons}}\left(\{y_i=0,p_{Ti}\};y_1=0,p_{T1};y_2=0,p_{T2}\right)\ = \\
&\Gamma^2 A_{n_1n_2}\left(2\to n|\{y_i=0,p_{Ti}\};y_1=0,\boldsymbol{p}_{T1}\right)A_{n_3n_4}\left(2\to n|\{y_i=0,p_{Ti}\};y_2=0,\boldsymbol{p}_{T2}\right)\ \to \qquad (9)\\
&A^{\text{identical gluons}}\left(\{y_i=0,p_{Ti}\};y_1=0,p_{T1};y_2=0,p_{T2}\right)\ = \\
&A^{\text{different gluons}}\left(\{0,p_{Ti}\};y_1=0,p_{T1};y_2=0,p_{T2}\right)\ +\ A^{\text{different gluons}}\left(\{0,p_{Ti}\};y_2=0,p_{T2};y_1=0,p_{T1}\right)\ = \\
&\qquad \Gamma^2 A_{n_1,n_2}\left(2\to n|\{y_i=0,p_{Ti}\};y_1=0,\boldsymbol{p}_{T1}\right)A_{n_3n_4}\left(2\to n|\{y_i=0,p_{Ti}\};y_2=0,\boldsymbol{p}_{T2}\right) \\
&\qquad +\ \Gamma^2 A_{n_1n_2}\left(2\to n|\{y_i=0,p_{Ti}\};y_2=0,\boldsymbol{p}_{T2}\right)A_{n_3n_4}\left(2\to n|\{y_i=0,p_{Ti}\};y_1=0,\boldsymbol{p}_{T1}\right)
\end{aligned}
$$

We wish to stress, that in Eq. (9) we use the Bose-Einstein symmetry for the production amplitudes, which are *only* functions of the transverse momenta of produced particles.

Such a replacement leads to the sum of the diagrams of Fig. 2-a and Fig. 2-b.

The goal of this paper is to calculate the function $C\left(R|\boldsymbol{p}_{T2}-\boldsymbol{p}_{T1}|\right)$ which tends to 1 at $\boldsymbol{p}_{T2}\to\boldsymbol{p}_{T1}$, and vanishes for $R|\boldsymbol{p}_{T2}-\boldsymbol{p}_{T1}|\gg 1$. To estimate $C\left(R|\boldsymbol{p}_{T2}-\boldsymbol{p}_{T1}|\right)$, it is sufficient to know the double inclusive cross section for $y_1=y_2$, where Fig. 2-b contributes significantly.

To obtain the double inclusive cross section, we need to add the cross section for two different gluon production which has the form

$$
\frac{d^2\sigma}{dy_1\,dy_2 d^2p_{T1}d^2p_{T2}}\ =\ \frac{d^2\sigma}{dy_1\,dy_2 d^2p_{T1}d^2p_{T2}}\left(\text{different gluons}\right)\left(1\ +\ \frac{1}{N_c^2-1}\ C\left(R|\boldsymbol{p}_{T2}-\boldsymbol{p}_{T1}|\right)\right) \qquad (10)
$$

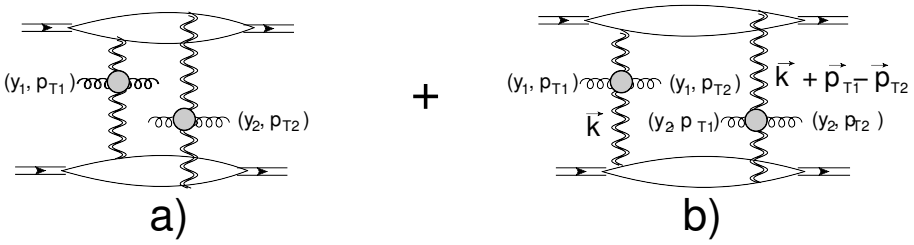

FIG. 2: Production of two identical gluons with $(y_1, \boldsymbol{p}_{T1})$ and $(y_2, \boldsymbol{p}_{T2})$ in two parton showers. The diagrams in the Mueller diagram technique [19] are shown in Fig. 2-a and Fig. 2-b. The wavy lines denote the BFKL Pomerons[20, 21].

In Eq. (10) we take into account, that we have $N_c^2 - 1$ pairs of the identical gluons, where N_c is the number of colours, and that the polarizations of the identical gluons should be the same. The latter leads to a suppression of $\frac{1}{2}$ of the second term in Eq. (10). Using Eq. (10) we can find v_n, since

$$\frac{d^2\sigma}{dy_1\, dy_2 d^2p_{T1} d^2p_{T2}} \;\propto\; 1 \;+\; 2\sum_n V_{n\Delta}\left(p_{T1}, p_{T2}\right)\cos\left(\Delta\,\varphi\right) \tag{11}$$

where $\Delta\varphi$ is the angle between $\boldsymbol{p}_{T1}$ and $\boldsymbol{p}_{T2}$. v_n is determined from $V_{n\Delta}\left(p_{T1}, p_{T2}\right)$

$$1.\;\; v_n\left(p_T\right) \;=\; \sqrt{V_{n\Delta}\left(p_T, p_T\right)}\,; \qquad\qquad 2.\quad v_n\left(p_T\right) \;=\; \frac{V_{n\Delta}\left(p_T, p_T^{\rm Ref}\right)}{\sqrt{V_{n\Delta}\left(p_T^{\rm Ref}, p_T^{\rm Ref}\right)}}\,; \tag{12}$$

Eq. (12)-1 and Eq. (12)-2 depict two methods of how the values of v_n have been extracted from the experimentally measured $V_{n\Delta}\left(p_{T1}, p_{T2}\right)$. $p_T^{\rm Ref}$ denotes the momentum of the reference trigger. These two definitions are equivalent if $V_{n\Delta}\left(p_{T1}, p_{T2}\right)$ can be factorized as $V_{n\Delta}\left(p_{T1}, p_{T2}\right) = v_n\left(p_{T1}\right) v_n\left(p_{T2}\right)$. We will show below that in our approach this is the case for the restricted kinematic region $R\, p_{Ti} \ll 1$.

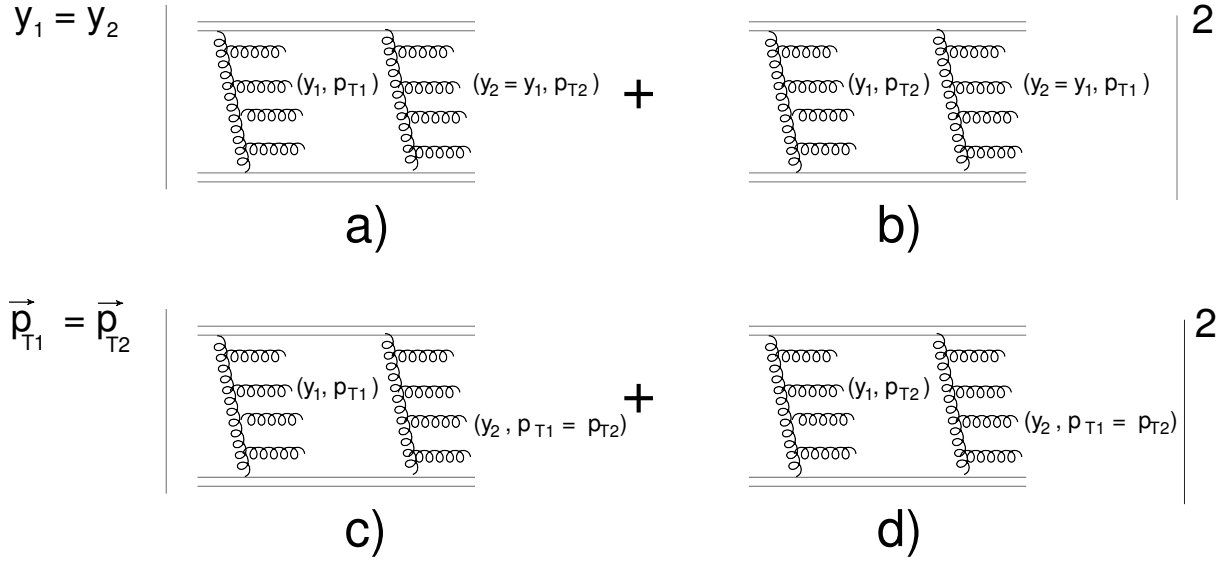

FIG. 3: The interferences between two states for the production of two identical gluons in two specific cases: $y_1 = y_2$ (Fig. 3-a and Fig. 3 -b) and $\boldsymbol{p}_{T1} = \boldsymbol{p}_{T2}$(Fig. 3-c and Fig. 3 -d).

The first problem that we face in calculating $C\left(R|\boldsymbol{p}_{T2} - \boldsymbol{p}_{T1}|\right)$, is to estimate the value of R, which increases with energy (see for example LHC data of Ref.[22]). On the other hand, the BFKL Pomeron[20, 21] does not lead to the shrinkage of the diffraction peak, as it has no slope for the Pomeron trajectory. The only way to obtain a size which increases with energy, is to use the unitarity constraints , $A^{\rm BFKL}\left(Y, b\right) \propto e^{\Delta_{\rm BFKL} Y} a(b) \,<\, 1$ [23], where $\Delta_{\rm BFKL}$ is the intercept of the BFKL Pomeron and b is the impact factor. However, in QCD $a\left(b\right)$ decreases as a power of b and the

unitarity constraints lead to $R \propto \exp(\Delta_{\rm BFKL} Y)$ [14]. Therefore, to obtain the energy behaviour of R, we need to introduce a non-perturbative correction at large b, which assures $a(b) \propto \exp(-\mu_{\rm soft} b)$, and also to take into account the multi Pomeron interactions which satisfy the unitarity constraints. Fortunately, the second part of the problem has been solved in the CGC/saturation approach[16], but the first needs modelling of the unknown confinement of quarks and gluons. Hence, we are doomed to build a model which includes everything that we know theoretically regarding the CGC/saturation approach, but in addition, one needs to introduce some phenomenological descriptions of the hadron structure, and the large b behaviour of the BFKL Pomeron.

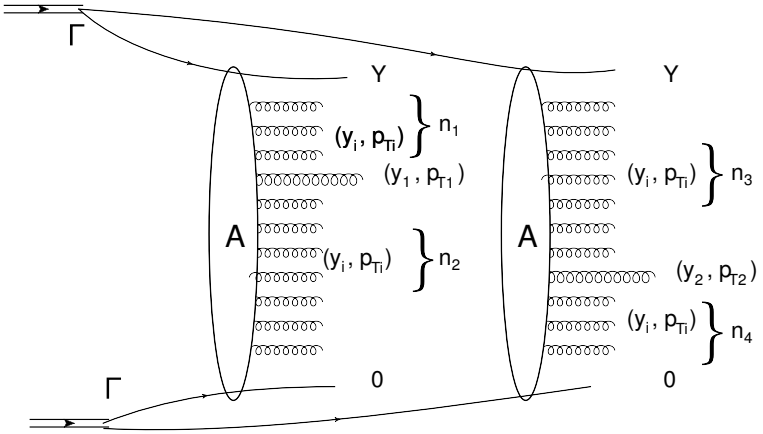

FIG. 4: The amplitude of production of $n = n_1 + n_2 + n_3 + n_4$ particles, $A^{\rm different\ gluons}(2 \to n|\{y_i, p_{Ti}\}; y_1, \boldsymbol{p}_{T1}; y_2, \boldsymbol{p}_{T2})$ (see Eq. (7a))

Such a model for hadron-hadron interactions at high energy has been developed in Refs.[25–28], and it successfully describes the experimental data on total, inelastic and diffractive cross sections, as well as the inclusive production and LRR correlations. The goal of this paper is to show that the structure of the 'dressed' Pomeron in this model leads to strong BE correlations, and generates v_n both for even and odd n, in hadron and nucleus interactions. In the next section we consider the contribution to $C(R|\boldsymbol{p}_{T2} - \boldsymbol{p}_{T1}|)$ from the first Mueller diagram, and discuss the different sources of BE-correlations. In section 3 we give a brief review of the structure of the Pomeron in our model, in which we incorporate the solution to the CGC/saturation equations with additional non-perturbative assumptions: the large b behaviour for the saturation momentum, and the structure of hadrons. It has been known for a long time [13, 29] in the framework of Gribov Pomeron calculus, and has been re-considered in CGC/saturation approach [30], that the LRR correlations stem from the production of gluon jets from two different parton showers (see Fig. 1). In section 4 we evaluate the BE correlations that result from the dressed Pomeron of our model, and show that they are able to describe the main features of the experimental data.

II. CALCULATION OF THE FIRST DIAGRAM

A. Proton-proton scattering

The first Mueller diagram which contributes to $C(R|\boldsymbol{p}_{T2} - \boldsymbol{p}_{T1}|)$ and which we need to calculate, is shown in Fig. 2-e and can be written in the form [31]:

$$\frac{d^2\sigma}{dy_1\, dy_2 d^2p_{T1} d^2p_{T2}} = \frac{d^2\sigma}{dy_1\, dy_2 d^2p_{T1} d^2p_{T2}}\,(\text{different gluons})\left(\frac{1}{N_c^2-1}\, C(R|\boldsymbol{p}_{T2} - \boldsymbol{p}_{T1}|)\right) \tag{13}$$

$$= \left(\frac{\bar{\alpha}_S\, C_F}{2\pi}\right)^2 \int d^2k_T\, N_{I\!P h}\left(k_T^2\right)\, N_{I\!P h}\left(\left(\boldsymbol{k_T} + \boldsymbol{p}_{T,12}\right)^2\right)\, \frac{d\sigma}{dy_1 d^2p_{T1}}\left(k_T, |\boldsymbol{k_T} + \boldsymbol{p}_{T,12}|\right)\, \frac{d\sigma}{dy_2 d^2p_{T2}}\left(k_T, |\boldsymbol{k_T} + \boldsymbol{p}_{T,12}|\right)$$

where $\boldsymbol{p}_{T,12} = \boldsymbol{p}_{T1} - \boldsymbol{p}_{T2}$ and

$$\frac{d\sigma}{dy_1 d^2p_{T1}}\left(k_T, |\boldsymbol{k_T} + \boldsymbol{p}_{T,12}|\right) = \int d^2q_T\, \phi^{\rm BFKL}\left(q_T, \boldsymbol{k}_T - \boldsymbol{q}_T\right)\, \Gamma_\mu\left(q_T, p_{T1}\right)\, \Gamma_\mu\left(\boldsymbol{k}_T - \boldsymbol{q}_T, p_{T2}\right)\, \phi^{\rm BFKL}\left(q_T, \boldsymbol{k}_T + \boldsymbol{p}_{T,12} - \boldsymbol{q}_T\right) \tag{14}$$

In Eq. (14) $\phi^{\rm BFKL}$ denotes the parton density of the BFKL Pomeron, with momentum transferred by the Pomeron $\boldsymbol{k}_T$ or $\boldsymbol{k}_T + \boldsymbol{p}_{T,12}$. The Lipatov vertex Γ_μ, as well as the equations for $\phi^{\rm BFKL}$ will be discussed in the appendix A. Generally speaking, $N_{I\!P h}$ has a structure which is shown in Fig. 5:

$$N_{I\!P h}\left(k_T^2\right) = \sum_{M_n}^{M_0} g^2_{I\!P n}\left(k_T^2\right)\delta\left(M^2 - M_n^2\right) + g_{I\!P h}\left(0\right) G_{3I\!P}\left(k_T^2\right) e^{\Delta_{\rm BFKL} Y} \tag{15}$$

where M_n denotes the mass of resonances, $\Delta_{\rm BFKL}$ the intercept of the BFKL Pomeron, and $G_{3I\!P}$ the triple Pomeron vertex. Considering the contribution of the first term to $N_{I\!P h}$, we can neglect, in the first approximation, the dependence of $\phi^{\rm BFKL}$ on the momentum transferred, since Q_T turns out to be of the order of the saturation momentum $Q_s \gg 1/R_h$, where R_h is the hadron size incorporated in $N_{I\!P h}$.

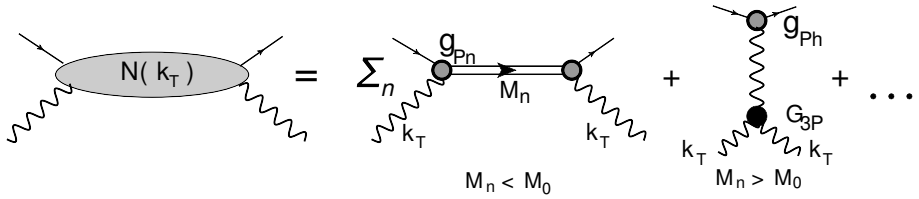

FIG. 5: The structure of $N_{I\!P h}\left(k_T^2\right)$.

This is not the case for the second term in Eq. (15), which has $Q_T \sim Q_s$. It leads to the BFKL Pomeron calculus which takes the Pomeron interactions into account. We will discuss this contribution in sections 3 and 4. In this section we restrict ourselves to the first term in the sum in Eq. (5). Collecting all formulae, we obtain that in the first diagram

$$C\left(R|\boldsymbol{p}_{T2} - \boldsymbol{p}_{T1}|\right) \propto \int d^2k_T\, g^2_{I\!P,\rm pr}\left(k_T^2\right)\, g^2_{I\!P,\rm tr}\left(\left(\boldsymbol{k} - \boldsymbol{p}_{T,12}\right)^2\right) \Big/ \int d^2k_T\, g^2_{I\!P,\rm pr}\left(k_T^2\right)\, g^2_{I\!P,\rm tr}\left(k_T^2\right) \tag{16}$$

To obtain the first estimates for the vertices of the soft Pomeron interaction with the projectile and target, we use the following parameterizations:

$$g_{pr}\left(k^2\right) = g^0_{pr}\, e^{-\frac{1}{2}B_{pr}\,k_T^2}; \qquad g_{tr}\left(k^2\right) = g^0_{tr}\, e^{-\frac{1}{2}B_{tr}\,k_T^2}; \tag{17}$$

For proton-proton collisions we take $B_{pr} = B_{tr} = B$.

In this case [1, 13]

$$C\left(R|\boldsymbol{p}_{T2} - \boldsymbol{p}_{T1}|\right) = \exp\left(-B_R\,\left(p_{T1}^2 - 2p_{T1}p_{T2}\cos\left(\Delta\varphi\right) + p_{T2}^2\right)\right) \tag{18}$$

with $B_R = B_{pr}B_{tr}/\left(B_{pr} + B_{tr}\right)$. $B_R = \frac{1}{2}B$ for proton-proton scattering.

In Ref.[1] it is shown that Eq. (18) leads to $V_{\Delta n}$ of Eq. (11) which is equal to

$$V_{\Delta\, n} = I_n\left(2B_R p_{T1}p_{T2}\right)\frac{e^{-B_R\left(p_{T1}^2 + p_{T2}^2\right)}}{N_C^2 - 1 + I_0\left(2B_R p_{T1}p_{T2}\right)\, e^{-B_R\left(p_{T1}^2 + p_{T2}^2\right)}} \tag{19}$$

where I_n is the modified Bessel function of the first kind.

In Fig. 6 taking $B_R = 5\,GeV^{-2}$, we plot the prediction for v_n using Eq. (19) and Eq. (12). This value of B_R, corresponds to the slope of the elastic cross section for proton-proton scattering at $W = 13\,GeV$. One can see that Eq. (12)-1 and Eq. (12)-2 give different predictions, demonstrating that we do not have factorization $V_{n\Delta}\left(p_{T1}, p_{T2}\right) \neq$

$v_n\,(p_{T1})\;v_n\,(p_{T2})$. Fig. 6-c shows v_n for $p_T^{\min} \le p_{T2} = p_T^{\rm Ref} \le p_T^{\max}$ with $p_T^{\min} = 0.5\,GeV$ and $p_T^{\max} = 5\,GeV$, as done in Ref.[10]. To calculate such a v_n, we need to know the dependence of the cross section on p_{T2}. Indeed, we need to take Eq. (10) and integrate it over p_{T2}: viz.

$$H\,(p_{T1},\Delta\varphi) \;=\; \int_{p_{T2}^{\min}}^{p_{T2}^{\max}} dp_{T2}^2\,\frac{d^2\sigma}{dy_1\,dy_2 d^2p_{T1}d^2p_{T2}}\,(Eq.\;(10)) \;\propto\; 1 \;+\; 2\sum_n V_{n\Delta}\,(p_{T1})\,\cos\,(\Delta\,\varphi) \tag{20}$$

For Fig. 6-c, we need to know the behaviour of the double inclusive cross section on p_{T1} and p_{T2}. We assume that $\frac{d^2\sigma}{dy_1\,dy_2\,d^2p_{T1}d^2p_{T2}} \propto 1\Big/\left(p_{T1}^2\,p_{T2}^2\right)$ for the cross sections given by Fig. 1-b and by Fig. 2-c and Fig. 2-d. In the appendix A we show that the cross section for Fig. 2-e $\frac{d^2\sigma}{dy_1\,dy_2\,d^2p_{T1}d^2p_{T2}}\,(Fig.\;2-e) \propto \left(1/p_{T1}^2 + 1/p_{T2}^2\right)^2$.

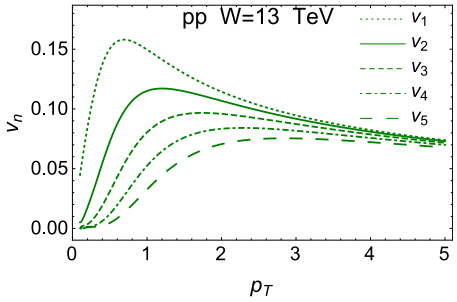

Fig. 6-a

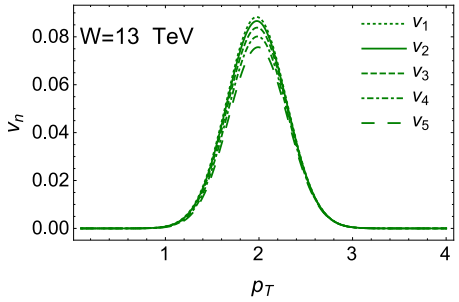

Fig. 6-b

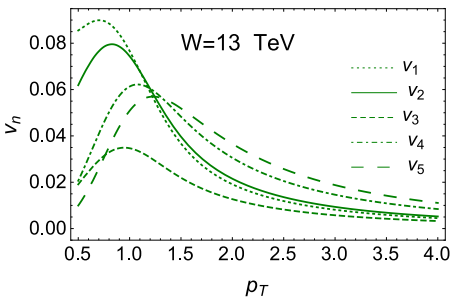

Fig. 6-c

FIG. 6: v_n versus p_T for proton-proton scattering at $W = 13\,TeV$, using Eq. (19) and Eq. (12). Fig. 6-a shows v_n that stem from Eq. (12)-1. In Fig. 6-b the estimates from Eq. (12)-2 for $p_T^{\rm Ref} = 2\,GeV$ are plotted. Fig. 6-c describes the same v_n as in Fig. 6-b, where, $p_T^{\rm Ref}$ is taken in the interval $0.5 - 5\,GeV$, as is measured in Ref.[10].

We took the energy dependence into account, by calculating the B_R from the slope of the elastic scattering at given energy W, which was taken from Ref.[25].

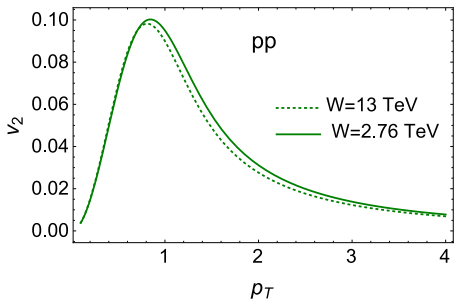

Fig. 7-a

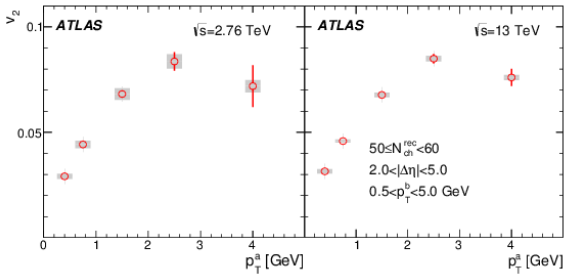

Fig. 7-b

FIG. 7: v_2 versus p_T for proton-proton scattering at $W = 2.76\,TeV$ and at $W = 13\,TeV$. Fig. 7-a shows v_n that stem from Eq. (12)-2 for $p_T^{\rm Ref}$ which is taken in the interval 0.5 to 5 GeV, as is measured in Ref.[10]. Fig. 7-b exhibits the experimental data taken from Ref.[10].

One can see that the calculated values, as well as energy dependence are close to the experimental data of Ref.[10]. The main difference is in the p_T dependence, which suggests the necessity to include the diffractive dissociation process or, in other words, the entire sum in Eq. (15), as well as the enhanced diagrams that are generated by the BFKL Pomeron calculus (see Fig. 5).

We can estimate the sum over resonances or, in other words, the diffraction production of states with low mass, by using our model (see appendix B for necessary formulae). In Fig. 8 we plot the correlation function $C\,(p_{T,12})$ as defined in Eq. (10) for $|\boldsymbol{p}_{T1}| = |\boldsymbol{p}_{T2}|$, which is the result of these calculations. One can see that the effective $p_{T,12}$ dependence of the slope, turns out to be much smaller than our estimates from the first diagrams that we obtained above. The slope that we used for the calculation shown in Fig. 6 was estimated as $\frac{1}{4}B_{el}$, where $B_{el} = 20\,GeV^{-2}$ is the slope of the elastic cross section at $W = 13\,TeV$. We see two reasons for such a drastic change in the $p_{T,12}$ dependence:

first, we took into account the diffractive production processes which were neglected in Fig. 6; and second, in our model the effective shrinkage of the diffraction peak originates from the shadowing corrections, as the BFKL Pomeron has no inherent shrinkage. Such corrections are stronger in net-diagrams of Fig. 14-b that are responsible for elastic scattering, than for the fan diagrams of Fig. 24 that contribute to inclusive production. Recall that $B_{\rm shr} \approx 10\,GeV^{-2}$ at $W = 13\,TeV$, comes from the shrinkage of the diffraction peak.

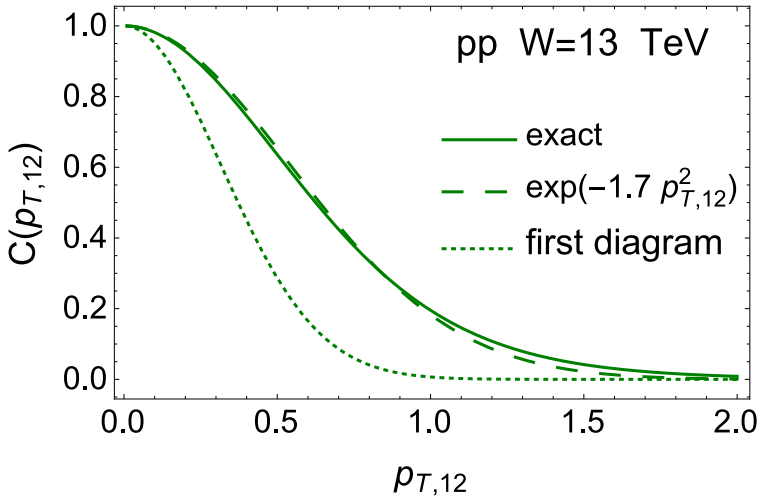

FIG. 8: Correlation function $C\left(p_{T,12}\right)$ as it is defined in Eq. (10), versus $p_{T,12} = |\boldsymbol{p}_{T1} - \boldsymbol{p}_{T2}|$. Dashed line corresponds to $\exp\left(-Bp^2_{T,12}\right)$ with $B = 1.7\,GeV^{-2}$, while the dotted line shows the dependence that we used in section 2 to calculate the first diagram: $\exp\left(-B\,p^2_{T,12}\right)$ with $B = 5\,GeV^{-2}$.

The calculation of v_n are shown in Fig. 9. One can see that we obtain large v_n for both odd and even n. The value of v_2 from Fig. 9-c is about 10% larger, than the experimental one from Ref.[10] (see Fig. 7-b). However, our calculations lead to narrower distributions in p_T than the experimental one. The factorization $V_{n\Delta}\left(p_{T1}, p_{T2}\right) = v_n\left(p_{T1}\right) v_n\left(p_{T2}\right)$ is strongly violated, as in the case of estimates of the first diagram.

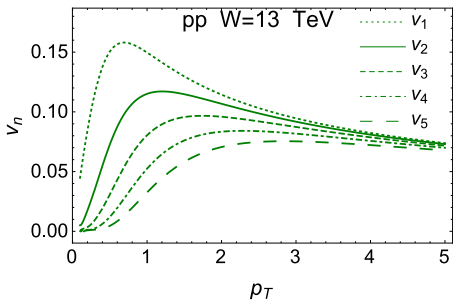

Fig. 9-a

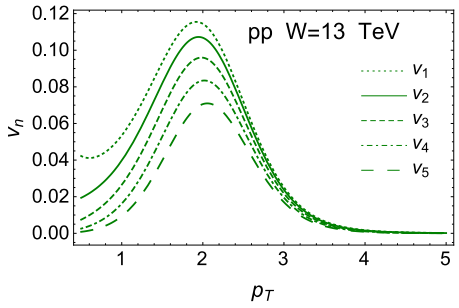

Fig. 9-b

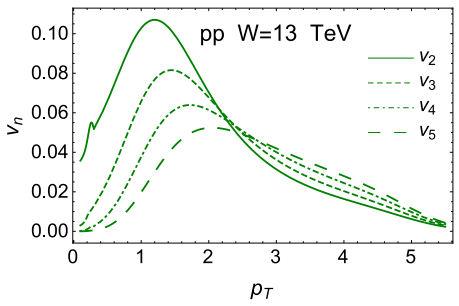

Fig. 9-c

FIG. 9: v_n versus p_T for proton-proton scattering at $W = 13\,TeV$, using Eq. (B9) and Eq. (12). Fig. 9-a shows v_n that stem from Eq. (12)-1. In Fig. 9-b the estimates from Eq. (12)-2 for $p_T^{\rm Ref} = 2\,GeV$ are plotted. Fig. 9-b describes the same v_n as in Fig. 6-c but $p_T^{\rm Ref}$ is taken in the interval 0.5 to 5 GeV, as is measured in Ref.[10].

Fig. 7 illustrates the energy dependence of v_n for proton-proton scattering, showing v_2 for two energies $W = 2.56\,TeV$ and $W = 13\,TeV$. Note, that v_2 does not depend on energy, in accord with the experimental data of Ref.[10].

Therefore, we can conclude that the first term in Eq. (15) leads to a value of v_n, which is large and of the order of the experimental one; the inclusion of diffraction in the region of small mass (sum over resonances in Eq. (15)) leads to a decrease of the interaction volume, but cannot reproduce the experimental p_T distributions of v_n, and BE correlations show the experimentally observed independence on energy.

B. Hadron-nucleus and nucleus nucleus interaction

For a nucleus we can simplify the calculation, considering cylindrical nuclei which have a form factor

$$S_A\left(k_T\right) \;=\; \frac{R_A}{k_T}\, J_1\left(k_T R_A\right) \tag{21}$$

where J_1 is the Bessel function. Taking Eq. (21) into account one can see that

$$\begin{aligned} C_{pA}\left(R|\boldsymbol{p}_{T2}-\boldsymbol{p}_{T1}|\right) \;&\propto\; \int d^2k_T\, g^2_{I\!P,\rm tr}\left(\left(\boldsymbol{k}_T-\boldsymbol{p}_{T,12}\right)^2\right)\, S^2_A\left(k^2_T\right) \Big/ \int d^2k_T\, g^2_{I\!P,\rm tr}\left(\left(k^2_T\right)^2\right)\, S^2_A\left(k^2_T\right) \\ &=\; \int d^2k_T\, e^{-B\left(k^2_T+p^2_{T,12}\right)}\, I_0\left(2B\, k_T\, p_{T,12}\right)\, S^2_A\left(k^2_T\right) \Big/ \int d^2k_T\; e^{-Bk^2_T}\; S^2_A\left(k^2_T\right) \end{aligned} \tag{22}$$

We expect that $S_A\left(k_T\right)$ leads to small $k_T \sim 1/R_A$, since the radius of nucleus is large. In Fig. 10-a we compare Eq. (22) with $\exp\left(-Bp^2_{T,12}\right)$ which follows from Eq. (22), replacing $S^2_A\left(k^2_T\right)$ by $\delta\left(k_T\right)$. The agreement is impressive.

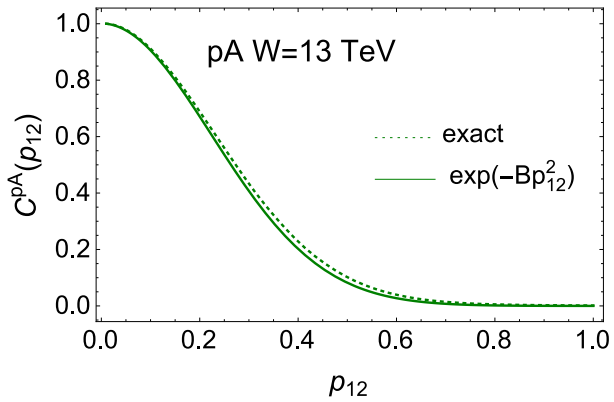

Fig. 10-a

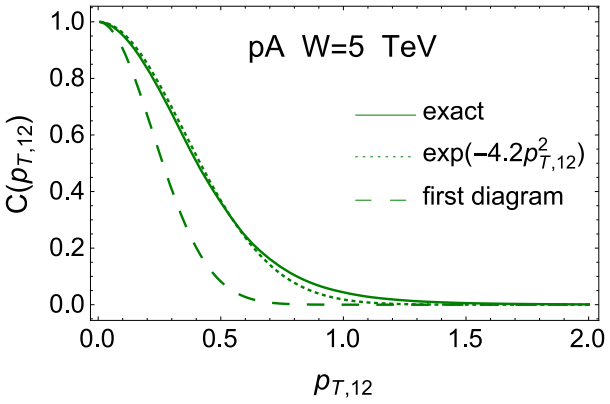

Fig. 10-b

FIG. 10: Fig. 10-a: comparison Eq. (22) with the same equation where $S^2_A\left(k^2_T\right)$ is replaced by $\delta\left(k_T\right)$. $R_A = 6.5fm$ for gold. $B = 10\,GeV^{-2}$ for proton at W =13 TeV. Fig. 10-b: correlation function $C\left(p_{T,12}\right)$ for proton-lead scattering at W = 5 TeV in our model (see appendix C) as it is defined in Eq. (10), versus $p_{T,12} = |\boldsymbol{p}_{T1} - \boldsymbol{p}_{T2}|$. Dashed line corresponds to $\exp\left(-Bp^2_{T,12}\right)$ with $B = 4.2\,GeV^{-2}$, while the dotted line shows the dependence that we used in section 2 to calculate the first diagram: $\exp\left(-B\,p^2_{T,12}\right)$ with $B = 10\,GeV^{-2}$

In Fig. 11 we plot the prediction for proton-gold scattering. One can see that the Bose-Einstein correlations generate large v_n for $n \geq 3$. Actually, we have several mechanisms (see, for example, review of Ref.[32]) for v_n with even n, therefore, it is instructive to note that the simple estimates in this section lead to large v_{2n-1}, larger than has been measured [11]. It should be stressed that using a more general approach which includes the diffractive production of small masses, as well as the shadowing corrections that lead to the shrinkage of diffractive peak, we obtain the predictions (see formulae in appendix C) which repeat the main features of our estimates in the simple model of Eq. (22). These calculations are plotted in Fig. 11-d - Fig. 11-f. In Fig. 10-b estimates for $C\left(p_{T,12}\right)$ in our model (see appendix C) are shown. One can see that $C\left(p_{T,12}\right)$ are different, and the model gives a smaller interaction volume. However, all qualitative features turn out to be the same: larger interaction volume than for proton-proton scattering, v_2 is much smaller than the experimental value (see Fig. 12); v_3, v_4 and even v_5 are close to the experimental values; and the value of the typical p_T is about $1\,GeV$ instead of $p_T = 3 - 4\,GeV$ in the experimental data.

For nucleus-nucleus interaction $C_{AA}\left(R|\boldsymbol{p}_{T2}-\boldsymbol{p}_{T1}|\right)$ takes the form

$$C_{AA}\left(R|\boldsymbol{p}_{T2}-\boldsymbol{p}_{T1}|\right) \;\propto\; \int d^2k_T\, S^2_A\left(\left(\boldsymbol{k}_T-\boldsymbol{p}_{T,12}\right)^2\right)\, S^2_A\left(k^2_T\right) \Big/ \int d^2k_T\, S^2_A\left(\left(k^2_T\right)^2\right)\, S^2_A\left(k^2_T\right) \tag{23}$$

Fig. 13 shows v_n for gold-gold scattering. One can see three major differences: v_n values turns out to be smaller than for proton-nucleus scattering, especially when $p_{T2} = p^{\rm Ref}_T$ differs from p_{T1}; the momentum distribution is much narrower than for pA scattering, and v_n are the same for all n.

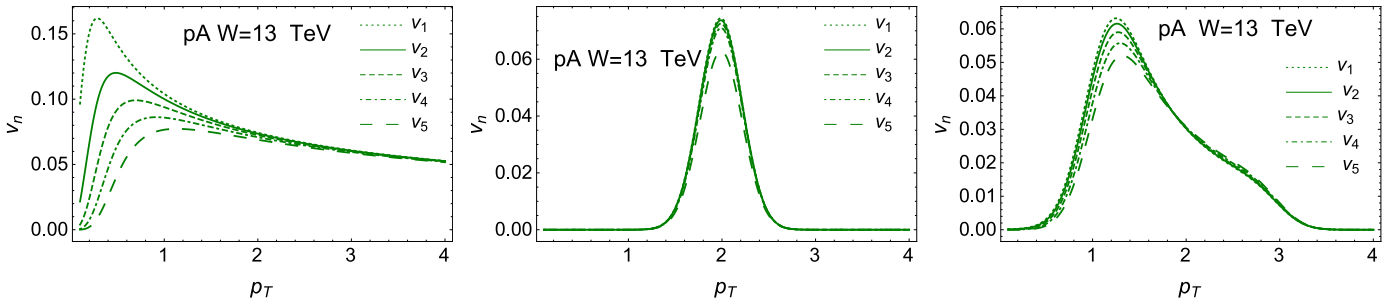

Fig. 11-a Fig. 11-b Fig. 11-c

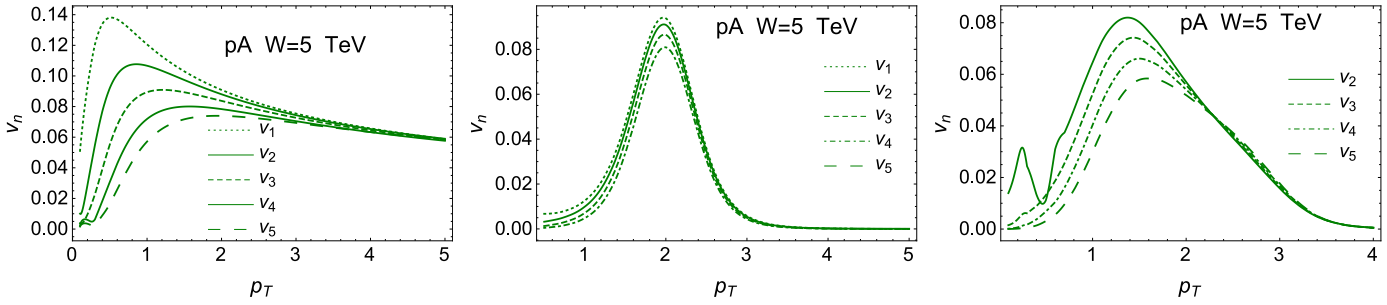

Fig. 11-d Fig. 11-e Fig. 11-f

FIG. 11: v_n versus p_T for proton - gold (Fig. 11-a - Fig. 11-c) scattering at $W = 13\,TeV$ and proton-lead scattering at $W = 5\,TeV$ (Fig. 11-d - Fig. 11-c), using Eq. (19) and Eq. (12). Fig. 11-a and Fig. 11-d show v_n that stem from Eq. (12)-1. In Fig. 11-b and Fig. 11-e the estimates from Eq. (12)-2 for $p_T^{\rm Ref} = 2\,GeV$ are plotted. Fig. 11-c and Fig. 11-f describe the same v_n as in Fig. 6-c but $p_T^{\rm Ref}$ is taken in the interval $1 - 3\,GeV$ as it is measured in Ref.[11].

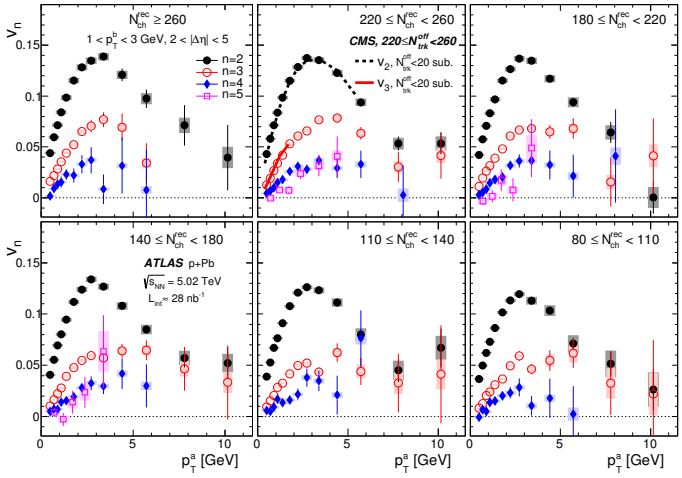

FIG. 12: v_n versus p_T for proton - lead scattering at $W = 5\,TeV$ measured by ATLAS collaboration[10] (Fig.9 from this paper)

Comparing Fig. 6, Fig. 11 and Fig. 13 we can conclude that the simplest estimates lead to sufficiently large v_n for both even and odd n, which are similar to those obtained in proton-proton and proton-nucleus collisions, but they are considerably smaller for the nucleus-nucleus case. Comparing these predictions with the experimental data of Refs.[2–12] we see that the BE correlations should be taken into account in all three reactions, since they give sizable contributions.

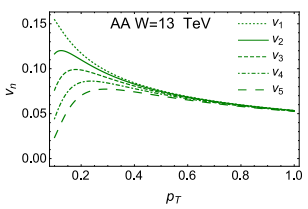

Fig. 13-a

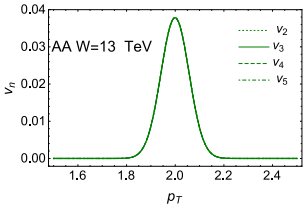

Fig. 13-b

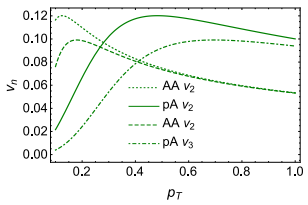

Fig. 13-c

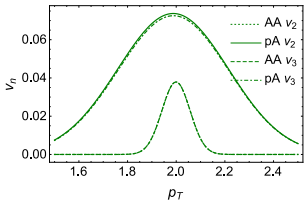

Fig. 13-d

FIG. 13: v_n versus p_T for gold - gold scattering at $W = 13\,TeV$, using Eq. (19) and Eq. (12). Fig. 13-a shows v_n that stem from Eq. (12)-1. In Fig. 13-b the estimates from Eq. (12)-2 for $p_T^{\rm Ref} = 2\,GeV$ is plotted. Fig. 13c and Fig. 13-d describe the difference between proton-gold and gold-gold interactions.

III. A BRIEF REVIEW OF OUR MODEL

In this section we will give a brief review of our model which has been developed in our papers [25, 26]. The advantage of the model is that it describes the experimental data on diffractive and elastic production[25]; the inclusive production [27] and large rapidity range (LRR) correlations [28].

As has been mentioned we need to build a model which incorporates at least two non-perturbative phenomena: the correct large b behaviour of the amplitude and the hadron structure. These need to be incorporated so as to reproduce in the framework of one approach, the main features of the experimental data, such as the increase of the interaction radius with energy, a sufficiently large cross section of diffraction production, as well as energy and multiplicity dependence of inclusive cross sections and two particle correlations. On the other hand, we wish to include as much information as possible from a theoretical approach based on QCD.

A. Theoretical input and 'dressed' Pomeron Green function

At the moment, the effective theory for QCD at high energies exists in two different formulations: the CGC/saturation approach [33–36], and the BFKL Pomeron calculus [20, 37–47]. In building our model we rely on the BFKL Pomeron calculus, since the relation to diffractive physics is more evident in this approach. However, we are aware that the CGC/saturation approach gives a more general pattern[45, 46]. In Ref.[46] it was proven that these two approaches are equivalent for

$$Y \leq \frac{2}{\Delta_{\rm BFKL}}\,\ln\left(\frac{1}{\Delta^2_{\rm BFKL}}\right) \tag{24}$$

where $\Delta_{\rm BFKL}$ denotes the intercept of the BFKL Pomeron. As we will see, in our model $\Delta_{\rm BFKL} \approx 0.2 - 0.25$ leading to $Y_{max} = 20 - 30$, which covers all accessible energies. In addition in Ref.[46] it is shown that for such Y, we can safely use the Mueller-Patel-Salam-Iancu (MPSI) approach[48], which allows us to calculate the contribution to the resulting BFKL Pomeron Green function (see Fig. 14-a):

$$\begin{aligned} &G^{\rm dressed}_{I\!P}\left(Y, r, R; b\right) \;=\; \\ &\int \prod_{i=1} d^2r_i\, d^2b_i\, d^2r'_i\, d^2b'_i\, N\left(Y - Y', r, \{r_i, b - b_i\}\right)\, A^{\rm BA}_{\text{dipole-dipole}}\left(r_i, r'_i, \boldsymbol{b}_i - \boldsymbol{b'}_i\right) N\left(Y', R, \{r'_i, b'_i\}\right) \end{aligned} \tag{25}$$

where $A^{BA}_{\text{dipole-dipole}}$ is the dipole-dipole scattering amplitude in the Born approximation of perturbative QCD, and is shown in Fig. 14-a by the red circles.

We need to find the amplitude for the production of dipoles of size r_i at impact parameters b_i. This amplitude can be written as (see Fig. 14-c)

$$\begin{aligned} &N\left(Y - Y', r, \{r_i, b_i\}\right) \;=\; \\ &\sum_{n=1}^{\infty} (-1)^{n+1}\, \widetilde{C}_n\left(\phi_0, r\right) \prod_{i=1}^{n} G_{I\!P}\left(Y - Y'; r, r_i, b_i\right) \;=\; \sum_{n=1}^{\infty} (-1)^{n+1}\, \widetilde{C}_n\left(\phi_0, r\right) \prod_{i=1}^{n} G_{I\!P}\left(z - z_i\right). \end{aligned} \tag{26}$$

$\widetilde{C}_n\left(\phi_0, r\right)$ is shown as the multi-Pomeron amplitudes (pink ovals) in Fig. 14-c.

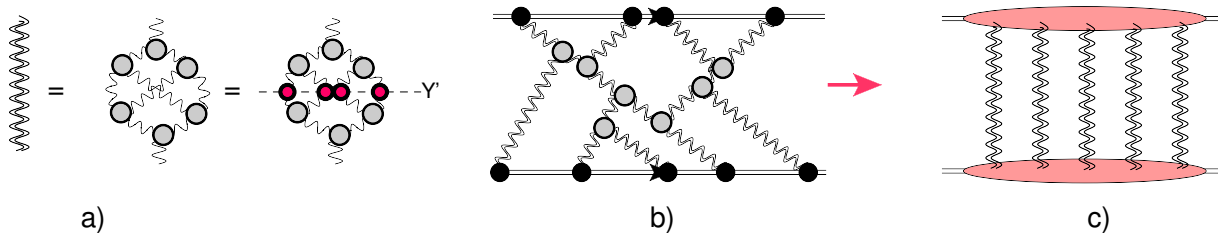

FIG. 14: Fig. 14-a shows the set of the diagrams in the BFKL Pomeron calculus that produce the resulting (dressed) Green function of the Pomeron in the framework of high energy QCD. The red blobs denote the amplitude of dipole-dipole interaction at low energy. In Fig. 14-b the net diagrams, which include the interaction of the BFKL Pomerons with colliding hadrons, are shown. The sum of the diagrams after integration over positions of $G_{3I\!P}$ in rapidity, reduces to Fig. 14-c.

The solution to the non-linear equation is of the following general form

$$N\left(G_{I\!P}\left(\phi_0, z\right)\right) \;=\; \sum_{n=1}^{\infty} \left(-1\right)^{n+1} C_n\left(\phi_0\right) G^n_{I\!P}\left(\phi_0, z\right). \tag{27}$$

Comparing Eq. (26) with Eq. (27) we see

$$\widetilde{C}_n\left(\phi_0, r\right) \;=\; C_n\left(\phi_0\right). \tag{28}$$

Coefficients C_n can be found from the solution to the Balitsky-Kovchegov equation [35] in the saturation region (see Ref.[47]).

$$N^{\rm BK}\left(G_{I\!P}\left(\phi_0, z\right)\right) \;=\; a\left(1 - \exp\left(-G_{I\!P}\left(\phi_0, z\right)\right)\right) \;+\; (1-a)\,\frac{G_{I\!P}\left(\phi_0, z\right)}{1 \,+\, G_{I\!P}\left(\phi_0, z\right)}, \tag{29}$$

with $a = 0.65$. Eq. (29) is a convenient parameterization of the numerical solution within accuracy better than 5%. Having C_n we can calculate the Green function of the dressed BFKL Pomeron using Eq. (25) and the property of the BFKL Pomeron exchange:

$$\begin{aligned} &\frac{\alpha_S^2}{4\pi}\, G_{I\!P}\left(Y - 0, r, R; b\right) \;= \\ &\int d^2r' d^2b'\, d^2r''\, d^2b''\, G_{I\!P}\left(Y - Y', r, r', \boldsymbol{b} - \boldsymbol{b}'\right)\; G_{I\!P}\left(Y' r'', R, \boldsymbol{b}''\right)\; A^{\rm BA}_{\text{dipole-dipole}}\left(r', r'', \boldsymbol{b''} - \boldsymbol{b'}\right) \end{aligned} \tag{30}$$

Carrying out the integrations in Eq. (25), we obtain the Green function of the dressed Pomeron in the following form:

$$\begin{aligned} G^{\rm dressed}\left(T\right) \quad &= \quad a^2(1 - \exp\left(-T\right)) + 2a(1-a)\frac{T}{1+T} + (1-a)^2 G\left(T\right) \\ \text{with} \quad &G\left(T\right) = 1 - \frac{1}{T}\exp\left(\frac{1}{T}\right)\Gamma\left(0, \frac{1}{T}\right) \end{aligned} \tag{31}$$

where $\Gamma\left(s, z\right)$ is the upper incomplete gamma function (see Ref.[60] formula **8.35**) and T is the BFKL Pomeron in the vicinity of the saturation scale

$$T\left(r_\perp, s, b\right) \;=\; \phi_0\left(r_\perp^2 Q_s^2\left(Y, b\right)\right)^{\bar{\gamma}} \tag{32}$$

B. Phenomenological assumptions and phenomenological parameters

The first phenomenological idea, is to fix the large impact parameter behaviour by assuming that the saturation momentum depends on b in the following way:

$$Q_s^2\left(b, Y\right) \;=\; Q_{0s}^2\left(b, Y_0\right)\, e^{\lambda\left(Y - Y_0\right)} \tag{33}$$

with

$$Q^2_{0s}\,(b,Y_0)\;=\;\left(m^2\right)^{1-1/\bar{\gamma}}\,\left(S\,(b,m)\right)^{1/\bar{\gamma}}\qquad S\,(b,m)\;=\;\frac{m^2}{2\pi}e^{-mb}\quad\text{and}\quad\bar{\gamma}\;=\;0.63 \tag{34}$$

We have introduced a new phenomenological parameter m to describe the large b behaviour. The Y dependence as well as r^2 dependence, can be found from CGC/saturation approach [16], since ϕ_0 and λ can be calculated in the leading order of perturbative QCD. However, since the higher order corrections turn out to be large [49] we treat them as parameters to be fitted. m is non-perturbative parameter which determines the typical sizes of dipoles inside hadrons. As one can see from Table 1 from the fit $m = 5.25$ GeV, supporting our main assumption that we can apply the BFKL Pomeron calculus, based on perturbative QCD, to the soft interaction since $m \gg \mu_{soft}$ where μ_{soft} is the scale of soft interaction, which is of the order of the mass of pion or $\Lambda_{\rm QCD}$.

Unfortunately, since the confinement problem is far from being solved, we have to assume a phenomenological approach for the structure of the colliding hadrons. We use a two channel model, which allows us to calculate the diffractive production in the region of small masses. In this model, we replace the rich structure of the diffractively produced states, by a single state with the wave function ψ_D, a la Good-Walker [50]. The observed physical hadronic and diffractive states are written in the form

$$\psi_h\;=\;\alpha\,\Psi_1+\beta\,\Psi_2\,;\qquad\psi_D\;=\;-\beta\,\Psi_1+\alpha\,\Psi_2;\qquad\text{where}\qquad\alpha^2+\beta^2\;=\;1; \tag{35}$$

Functions ψ_1 and ψ_2 form a complete set of orthogonal functions $\{\psi_i\}$ which diagonalize the interaction matrix T

$$A^{i'k'}_{i,k}\;=<\psi_i\,\psi_k|\mathbf{T}|\psi_{i'}\,\psi_{k'}>=A_{i,k}\,\delta_{i,i'}\,\delta_{k,k'}. \tag{36}$$

The unitarity constraints take the form

$$2\,\mathrm{Im}\,A_{i,k}\,(s,b)=|A_{i,k}\,(s,b)\,|^2+G^{in}_{i,k}(s,b), \tag{37}$$

where $G^{in}_{i,k}$ denotes the contribution of all non diffractive inelastic processes, i.e. it is the summed probability for these final states to be produced in the scattering of a state i off a state k. In Eq. (37) $\sqrt{s} = W$ denotes the energy of the colliding hadrons, and b the impact parameter. A simple solution to Eq. (37) at high energies, has the eikonal form with an arbitrary opacity Ω_{ik}, where the real part of the amplitude is much smaller than the imaginary part.

$$A_{i,k}(s,b)=i\left(1-\exp\left(-\Omega_{i,k}(s,b)\right)\right), \tag{38}$$

$$G^{in}_{i,k}(s,b)=1-\exp\left(-2\,\Omega_{i,k}(s,b)\right). \tag{39}$$

Eq. (39) implies that $P^S_{i,k} = \exp\left(-2\,\Omega_{i,k}(s,b)\right)$, is the probability that the initial projectiles (i,k) reach the final state interaction unchanged, regardless of the initial state re-scatterings.

C. Small parameters from the fit and the scattering amplitude

The first approach is to use the eikonal approximation for Ω in which

$$\Omega_{i,k}(r_\perp,Y-Y_0,b)\;=\;\int d^2b'\,d^2b''\,g_i\left(\boldsymbol{b}'\right)\,G^{\rm dressed}\left(T\left(r_\perp,Y-Y_0,\boldsymbol{b}''\right)\right)\,g_k\left(\boldsymbol{b}-\boldsymbol{b}'\;-\boldsymbol{b}''\right) \tag{40}$$

We propose a more general approach, which takes into account new small parameters, that come from the fit to the experimental data (see Table 1 and Fig. 14 for notations):

$$G_{3I\!P}\Big/g_i(b=0)\;\ll\;1;\qquad m\;\gg\;m_1\text{ and }m_2 \tag{41}$$

The second equation in Eq. (41) leads to the fact that b'' in Eq. (40) is much smaller than b and b', therefore, Eq. (40) can be re-written in a simpler form

$$\begin{aligned}\Omega_{i,k}(r_\perp,Y-Y_0,b)\;&=\;\left(\int d^2b''\,G^{\rm dressed}\left(T\left(r_\perp,Y-Y_0,\boldsymbol{b}''\right)\right)\right)\int d^2b'g_i\left(\boldsymbol{b}'\right)\,g_k\left(\boldsymbol{b}-\boldsymbol{b}'\right)\\&=\;\tilde{G}^{\rm dressed}\left(r_\perp,Y-Y_0\right)\,\int d^2b'g_i\left(\boldsymbol{b}'\right)\,g_k\left(\boldsymbol{b}-\boldsymbol{b}'\right)\end{aligned} \tag{42}$$

Using the first small parameter of Eq. (41), we can see that the main contribution stems from the net diagrams shown in Fig. 14-b. The sum of these diagrams[25] leads to the following expression for $\Omega_{i,k}(s,b)$

$$\Omega\left(r_\perp, Y-Y_0; b\right) = \int d^2b' \; \frac{g_i\left(\boldsymbol{b}'\right)\, g_k\left(\boldsymbol{b}-\boldsymbol{b}'\right)\, \tilde{G}^{\rm dressed}\left(r_\perp, Y-Y_0\right)}{1 \,+\, G_{3I\!P}\, \tilde{G}^{\rm dressed}\left(r_\perp, Y-Y_0\right)\left[g_i\left(\boldsymbol{b}'\right)+g_k\left(\boldsymbol{b}-\boldsymbol{b}'\right)\right]}; \tag{43}$$

$$g_i\left(b\right) = g_i\, S_p\left(b; m_i\right); \tag{44}$$

where

$$S_p\left(b, m_i\right) \,=\, \frac{1}{4\pi} m_i^3\, b\, K_1\left(m_i b\right) \tag{45}$$

$$\tilde{G}^{\rm dressed}\left(r_\perp, Y-Y_0\right) \,=\, \int d^2b\; G^{\rm dressed}\left(T\left(r_\perp, Y-Y_0, b\right)\right) \tag{46}$$

where $T\left(r_\perp, Y-Y_0, b\right)$ is given by Eq. (32).

Note that $\tilde{G}^{\rm dressed}\left(Y-Y_0\right)$ does not depend on b. In all previous formulae, the value of the triple BFKL Pomeron vertex is known: $G_{3I\!P} = 1.29\, GeV^{-1}$.

model	λ	$\phi_0\ (GeV^{-2})$	$g_1\ (GeV^{-1})$	$g_2\ (GeV^{-1})$	$m(GeV)$	$m_1(GeV)$	$m_2(GeV)$	β	$a_{I\!P I\!P}$
2 channel	0.38	0.0019	110.2	11.2	5.25	0.92	1.9	0.58	0.21

TABLE I: Fitted parameters of the model. The values are taken from Ref.[25].

To simplify further discussion, we introduce the notation

$$N^{BK}\left(G^i_{I\!P}\left(r_\perp, Y, b\right)\right) \,=\, a\,\left(1-\exp\left(-G^i_{I\!P}\left(r_\perp, Y, b\right)\right)\right) \,+\, (1-a)\,\frac{G^i_{I\!P}\left(r_\perp, Y, b\right)}{1 \,+\, G^i_{I\!P}\left(r_\perp, Y, b\right)}, \tag{47}$$

with $a = 0.65$. Eq. (47) is an analytical approximation to the numerical solution for the BK equation[47]. $G^i_{I\!P}\left(r_\perp, Y; b\right) \,=\, g_i\left(b\right)\, \tilde{G}^{\rm dressed}\left(r_\perp, Y-Y_0\right)$. We recall that the BK equation sums the 'fan' diagrams.

For the elastic amplitude we have

$$a_{el}(b) \,=\, \left(\alpha^4 A_{1,1} \,+\, 2\alpha^2\,\beta^2\, A_{1,2} \,+\, \beta^4 A_{2,2}\right). \tag{48}$$

We will discuss the inclusive production as well as LRR correlations in appendix B.

IV. AZIMUTHAL ANGLE CORRELATION AND THE STRUCTURE OF THE 'DRESSED' POMERON

As has been discussed, our model includes three dimensional scales: m,m_1 and m_2. m_1 and m_2 describe two typical sizes in the proton wave function, which could be associated with the distance between constituent quarks (size of proton) $R_p \sim 1/m_1$ and the size of the constituent quark $R_q \sim 1/m_2$ in the framework of the constituent quark model [55]. The third scale: m, characterizes the impact parameter behaviour of the saturation scale, and is intimately related to the structure of the dressed Pomeron in our model. In section 2 we discussed how two scales in the proton wave function arise in the BE correlations. Here, we would like to show that the third scale leads to the BE correlations which can explain the values of v_n observed experimentally.

As we have discussed in section 3-A , the dressed Pomeron is the sum of enhanced diagrams (see Fig. 14-a) which is given by Eq. (31). Therefore, the exchange of the dressed Pomeron generates the production of an infinite number of the parton showers and, in particular, two parton showers which generate the BE correlations as is shown in Fig. 15. Integration over rapidities of triple Pomeron vertices[44] reduces the diagrams of Fig. 15-a and Fig. 15-b to the diagrams of Fig. 15-c and Fig. 15-d. We can calculate the probability to find two parton showers (P_2) inside of the dressed Pomeron expanding Eq. (31):

$$P_2 \,=\, (2 - 2a + a^2/3) \,=\, 0.91 \quad \text{for} \quad a = 0.65 \tag{49}$$

and the contribution of two parton showers production to the double inclusive cross section for the diagrams of Fig. 15-a, is equal to

$$\frac{d^2\sigma}{dy_1\,dy_2 d^2p_{T1} d^2p_{T2}} \;=\; a^2_{I\!P I\!P}\,P_2^2\int d^2k_T\;T\left(k_T, Y-y_1\right)\,T\left(k_T, Y-y_2\right)\,T\left(k_T, y_1\right)\,T\left(k_T,\;y_2\right) \tag{50}$$

where $a_{I\!P I\!P}$ denotes the Mueller vertex of gluon emission (see Fig. 15). In our estimates for the calculation of v_n, we do not need to know the probability P_2, as well as the vertex $a_{I\!P I\!P}$, assuming that $a_{I\!P I\!P}$ is the same in Fig. 15-a and in Fig. 15-b. In Eq. (50) all rapidities are in the laboratory frame.

$T\left(k_T, y\right)$ is the Fourier image of $T\left(b, y\right)$ defined in Eq. (32)-Eq. (34) and it takes the form

$$T\left(k_T, y\right) \;=\; \phi_0\,\frac{1}{\left(1+\frac{k_T^2}{m^2}\right)^{3/2}}\,e^{\lambda\,\bar{\gamma}\left(Y-Y_0\right)} \tag{51}$$

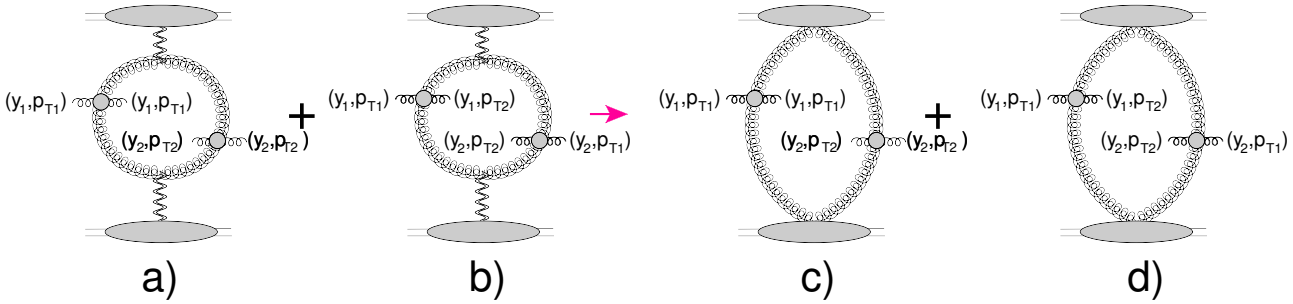

FIG. 15: The Mueller diagrams for the BE correlation for the 'dressed' Pomeron. A blob denotes the vertex for gluon emission $a_{I\!P I\!P}$ (see Eq. (50)).

For the interaction with nuclei, we need to take into account the interaction of the Pomeron with the nucleons inside the nucleus, as it is shown in Fig. 16. The equation for the resulting $T_A\left(y, k_T\right)$ takes the form (see Fig. 17-a)

$$T_A\left(y, k_T\right) \;=\; T\left(y, k_T\right) \;-\; \Gamma_{3I\!P}\int_0^y dy'\,T\left(y-y', k_T\right)\int d^2k'_T\,G_A\left(y'\boldsymbol{k}-\boldsymbol{k}'\right)\,T_A\left(y', k'_T\right) \tag{52}$$

The triple Pomeron vertex $\Gamma_{3I\!P}$ will be calculated in our model below.

The typical $|\boldsymbol{k}-\boldsymbol{k}'| \sim 1/R_A \;\ll\; 1/m$ and, therefore, we can replace $G_A\left(y', \boldsymbol{k}-\boldsymbol{k}'\right)$ by $\widetilde{G}_A\left(y'\right)\delta^{(2)}\left(\boldsymbol{k}-\boldsymbol{k}'\right)$. Note that the normalization is such that the first diagram for $\widetilde{G}_A \;=\; S_A\left(b=0\right)T\left(y, k_T=0\right)$, where $S_A\left(b\right)$ is defined in Eq. (C4). After integration over k'_T, Eq. (52) reduces to the following equation

$$T_A\left(y, k_T\right) \;=\; T\left(y, k_T\right) \;-\; \Gamma_{3I\!P}\int_0^y dy'\,T\left(y-y', k_T\right)\widetilde{G}_A\left(y'\right)\,T_A\left(y', k'_T\right) \tag{53}$$

For $\widetilde{G}_A$ we have the equation of Fig. 17-b, which has the following analytical form:

$$\widetilde{G}_A\left(y\right) \;\;=\;\; S_A\left(b=0\right)\,T\left(y, k_T=0\right) \;-\; \Gamma_{3I\!P}\int_0^y dy'\;T\left(y-y', k_T\right)\widetilde{G}^2_A\left(y'\right) \tag{54}$$

The solution to these two equations (Eq. (53) and Eq. (54) can be written as follows

$$T_A\left(y, k_T\right) \;=\; \frac{T\left(y, k_T\right)}{1+\tilde{\Gamma}_{3I\!P}\,S_A\left(b=0\right)\,T\left(y, k_T\right)} \tag{55}$$

where $\tilde{\Gamma}_{3I\!P} = \Gamma_{3I\!P}/\left(\lambda\,\bar{\gamma}\right) \;=\; P_2$.

$T\left(y, k_T\right)$ has a physical meaning, of the BFKL amplitude in the vicinity of the saturation scale, where it has a geometric scaling behaviour [56], and it depends on one variable $z = \ln\left(r^2Q_s^2(Y)\right)$. For diagrams of Fig. 15 the typical $r \sim 1/m_i$ and $z \to \lambda Y$. It is well known that the main contribution to the inclusive cross section stems from vicinity of the saturation scale, since this cross section is proportional to $\nabla^2_r N\left(r, b; Y\right)$, which tends to zero inside the saturation

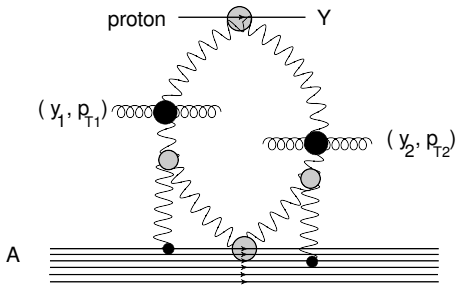

FIG. 16: The Mueller diagrams for the BE correlation for the 'dressed' Pomeron for proton-nucleus scattering. Black blob denotes the vertex for gluon emission $a_{I\!P I\!P}$ (see Eq. (41), the gray blob stands for the triple Pomeron vertex.

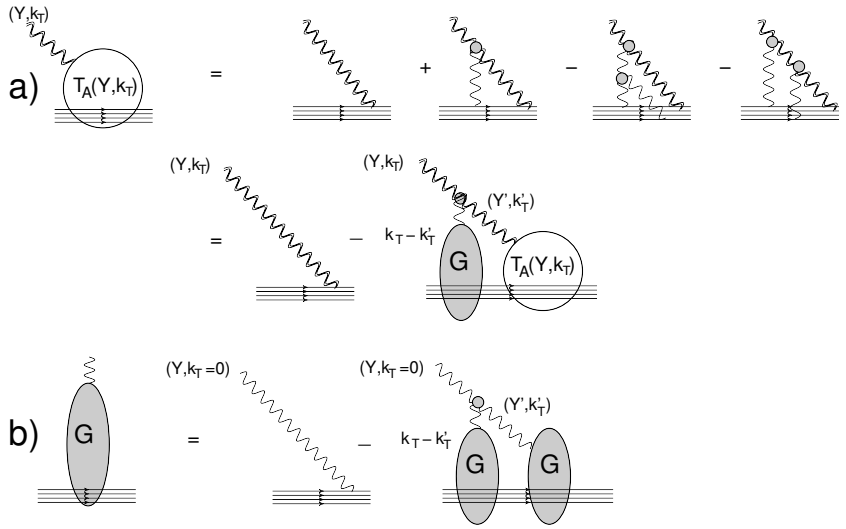

FIG. 17: Graphic form of equation for $T_A\left(y, k_T\right)$. The wavy double lines denote $T\left(Y, k_T\right)$ of Eq. (51), while the wavy lines stand for $T_A\left(y, k_T = 0\right)$.

domain (see Eq. (A9)). N is the scattering amplitude of the dipole with size r. The fact that we are dealing with the amplitude in the region where it has geometric scaling behaviour, is the reason why a non-linear equation of the BK type [35] is degenerate to one dimensional equations (see Eq. (53) - Eq. (55)).

Using Eq. (50) we can calculate $C\left(|\boldsymbol{p}_{T1} - \boldsymbol{p}_{T2}|\right)$ for proton-proton scattering, given by Eq. (1) which is equal to

$$C_{\rm pp}\left(|\boldsymbol{p}_{T1} - \boldsymbol{p}_{T2}|\right) = \frac{1}{N_c^2 - 1}\frac{\int d^2k_T\; T\left(k_T, Y - y_1\right)\; T\left(k_T, Y - y_2\right)\; T\left(\boldsymbol{k}_T - \boldsymbol{p}_{T,12}, y_1\right)\; T\left(\boldsymbol{k}_T - \boldsymbol{p}_{T,12},\; y_2\right)}{\int d^2k_T\; T\left(k_T, Y - y_1\right)\; T\left(k_T, Y - y_2\right)\; T\left(k_T, y_1\right)\; T\left(k_T,\; y_2\right)} \tag{56}$$

For proton-nucleus we have

$$C_{\rm pA}\left(|\boldsymbol{p}_{T1} - \boldsymbol{p}_{T2}|\right) = \frac{1}{N_c^2 - 1}\frac{\int d^2k_T\; T_A\left(k_T, Y - y_1\right)\; T_A\left(k_T, Y - y_2\right)\; T\left(\boldsymbol{k}_T - \boldsymbol{p}_{T,12}, y_1\right)\; T\left(\boldsymbol{k}_T - \boldsymbol{p}_{T,12},\; y_2\right)}{\int d^2k_T\; T\left(k_T, Y - y_1\right)\; T\left(k_T, Y - y_2\right)\; T\left(k_T, y_1\right)\; T\left(k_T,\; y_2\right)} \tag{57}$$

and for nucleus - nucleus $C_{\rm AA}$ has the form:

$$C_{\rm AA}\left(|\boldsymbol{p}_{T1} - \boldsymbol{p}_{T2}|\right) = \frac{1}{N_c^2 - 1}\frac{\int d^2k_T\; T_A\left(k_T, Y - y_1\right)\; T_A\left(k_T, Y - y_2\right)\; T_A\left(\boldsymbol{k}_T - \boldsymbol{p}_{T,12}, y_1\right)\; T_A\left(\boldsymbol{k}_T - \boldsymbol{p}_{T,12},\; y_2\right)}{\int d^2k_T\; T\left(k_T, Y - y_1\right)\; T\left(k_T, Y - y_2\right)\; T\left(k_T, y_1\right)\; T\left(k_T,\; y_2\right)} \tag{58}$$

The results of calculations for $C\left(R_{\rm cor}p_{T,12}\right)$ using Eq. (56) - Eq. (58) are plotted in Fig. 18, One can see that the radius of correlations ($R^2_{\rm cor} = B$) turns out to be very small in comparison with the same radius in Fig. 8 and Fig. 10.

From $C\left(R_{\rm cor}p_{T,12}\right)$ we can calculate v_n using Eq. (11) and Eq. (12)-1. However, $C\left(R_{\rm cor}p_{T,12}\right)$ shown in Fig. 18, are calculated for the production of gluon jets, while experimentally v_n are measured for a hadron. Following Ref. [57] we explore the local parton-hadron duality(LPHD) suggested in Ref. [58].

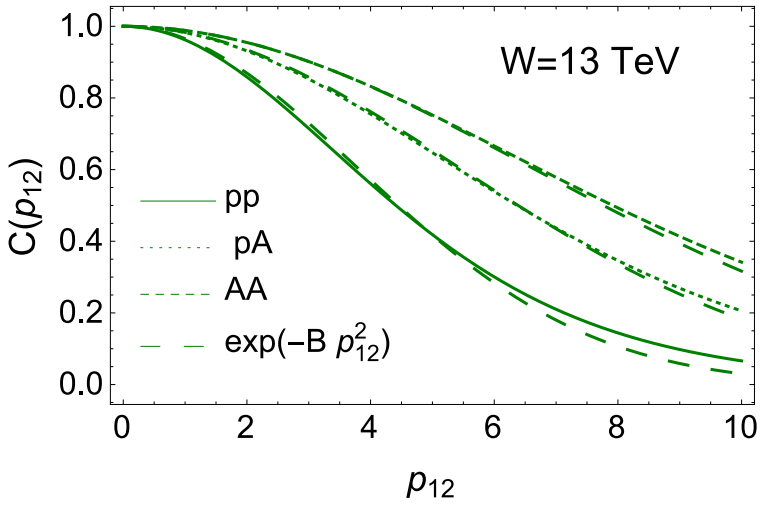

FIG. 18: $C\left(|\boldsymbol{p}_{T1}-\boldsymbol{p}_{T2}|=p_{T,12}\right)$, calculated using Eq. (56) - Eq. (58), versus $p_{T,12}$ for three reactions: proton-proton, proton - lead and lead - lead collisions at energy $W = 13\,TeV$. The long dashed curves correspond to $\exp\left(-B\,p_{T,12}^2\right)$ with $B_{\rm pp} = 0.035\,GeV^{-2}$, $B_{\rm pA} = 0.027\,Ge4V^{-2}$ and $B_{\rm AA} = 0.022\,GeV^{-2}$.

In our approach the hadrons originate from the decay of a gluon jet, and their transverse momenta are

$$\boldsymbol{p}_{\rm hadron,\,T} \;=\; z\,\boldsymbol{p}_{\rm jet,\,T} \;+\; \boldsymbol{p}_{\rm intristic,\,T} \tag{59}$$

where z is the fraction of energy of the jet, carried by the hadron. $\boldsymbol{p}_{\rm intristic,\,T}$ is the transverse momentum of the hadron in the mini-jet that has only longitudinal momentum. From Eq. (59) we obtain that the average p_T of hadrons is equal to

$$\langle p_{\rm hadron,\,T}\rangle \;=\; \sqrt{z^2\,p^2_{\rm jet,\,T} \;+\; p^2_{\rm intristic,\,T}} \tag{60}$$

In Ref.[57] we found that we need to take $z = 0.5$ and $p_{\rm intristic,\,T} = m_\pi$, to describe the inclusive spectra of hadron at the LHC. Using Eq. (60) we recalculate v_n for a gluon jet to v_n for hadrons, which are shown in Fig. 19. Comparing with the experimental data [2–12], and Fig. 7-b and Fig. 12, one can see that we describe the proton-proton scattering rather well, while for proton-nucleus we obtain v_2 which is smaller by 15- 20%. For lead-lead collisions v_2 turns out to be two times smaller than the experimental value [12]. However, for central events with centrality 0 - 10% measured v_2 is very close to our estimates. v_n with $n \geq 3$ are larger than the experimental values. In general the p_T distribution is wider than the experimental one. The LPHD approach and Eq. (60) are very approximate, and we need to use a more advanced jet fragmentation function. Second, we need to add together the two mechanisms: one discussed in this section and one discussed in section 2. We need to include a more advanced fragmentation function, together with more careful accounting of the emission vertex in QCD (see appendix A). We will consider these in a future publication.

The estimates from our model show that the mechanism that has been discussed in section 2, yields about 10 -20% of the contribution which we now consider. In Fig. 20 one can see how the sum of two mechanism occur in v_2. One can see that the sum has a wider p_T distribution and a smaller maximal value. For proton-proton collisions both effects make predictions closer to the experimentally observed values of v_2 [10].

One of the properties that has been violated in the estimates in section 2, was the factorization $r_n = 1$ where

$$r_n \;=\; \frac{V_{n\Delta}\left(p_{T1},p_{T2}\right)}{\sqrt{V_{n\Delta}\left(p_{T1},p_{T1}\right)\,V_{n\Delta}\left(p_{T2},p_{T2}\right)}} \;=\; 1 \tag{61}$$

Fig. 21 shows that Eq. (61) holds at least for $p_T \leq 4\,GeV$ in accordance with the experimental data (see Ref.[11]).

V. CONCLUSIONS

In this paper we showed how three different dimensional scales in high energy scattering, arise in the Bose-Einstaein correlations that generates v_n, for even and odd n. The first two scales are intimately related to the structure of the

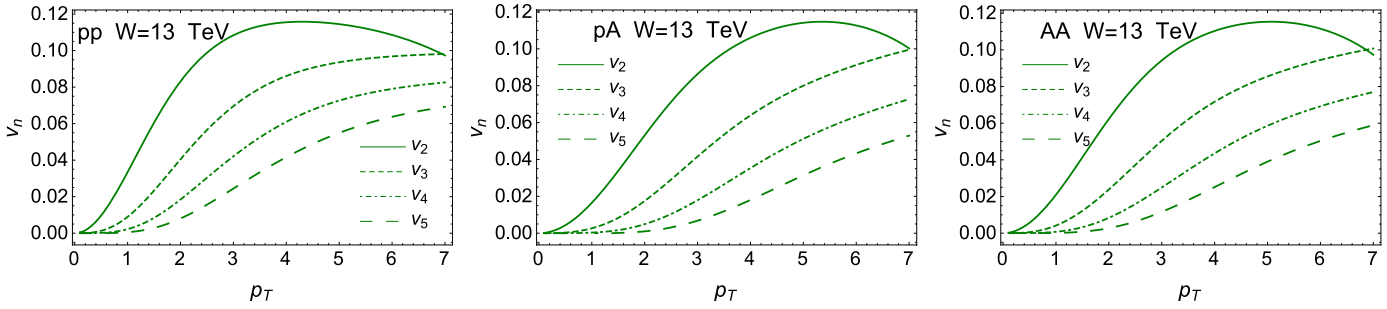

Fig. 19-a Fig. 19-b Fig. 19-c

FIG. 19: v_n versus p_T at $W = 13\,TeV$ for proton-proton (Fig. 19-a), proton-lead (Fig. 19-b) and lead-lead (Fig. 19-c) scatterings, using Eq. (11) and Eq. (12)-1.

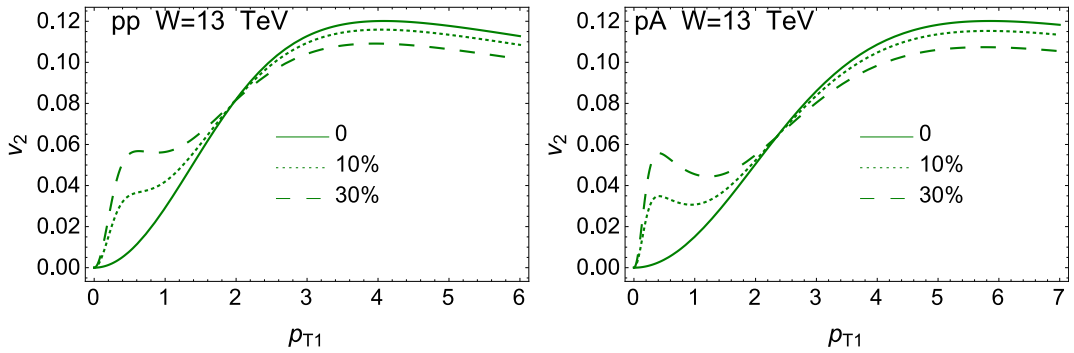

Fig. 20-a Fig. 20-b

FIG. 20: v_2 versus p_T at $W = 13\,TeV$ for proton-proton (Fig. 20-a) and proton-lead (Fig. 20-b) for the sum of two contributions: the 'dressed' Pomeron structure and the diffractive production, discussed in section 2. The percents indicate the fraction of diffractive production in the Pomeron structure.

wave function of the hadron, and have an interpretation in the constituent quark model, as the distance between the constituent quarks and the size of the quark. In a more formal way they characterize the size of the vertex of the BFKL Pomeron interaction with the hadron, and the typical size of the same vertex for the diffraction production, in the region of small mass. We demonstrated that these sizes lead to BE correlations which are large, but narrowly distributed in p_T .

The third size is the value of the saturation momentum in the CGC/saturation approach, and has been used in the construction of our model for the high energy soft interactions. This size is incorporated in the structure of the 'dressed' Pomeron in our model. It turns out that this size leads to values of v_n which are close to the experimental values both for even and odd n, and they are broadly distributed in p_T. In proton-proton scattering this mechanism is able to describe the experimental data both for even and odd v_n, while for proton-nucleus and nucleus-nucleus collisions we obtain smaller values of v_2: 20-30% smaller for proton-lead scattering, and two times smaller for lead-lead collisions. However, we would like to stress that for centrality 0-10%, the structure of the Pomeron gives values of v_n which are very close to the experimentally observed ones.

All estimates were made in the framework of our model for soft interactions which is based on CGC/saturation approach, but introduces non-perturbative parameters which describe the wave function of the hadron, and the large impact parameter behaviour of the saturation momentum. We describe in this model the total, elastic and diffractive cross sections as well as the inclusive production and long range rapidity correlations, and therefore, we trust that we can rely on the model when discussing the azimuthal angle correlations.

We demonstrated in this paper that BE correlations in the framework of CGC/saturation approach are able to explain a substantial part if not the entire, experimental values of v_n for both even and odd n. Therefore, we believe that is premature to conclude that the origin of the observed long range rapidity correlations are only due to elliptic flow.

Acknowledgements We thank our colleagues at Tel Aviv University and UTFSM for encouraging discussions. Our special thanks go to Carlos Cantreras, Alex Kovner and Michel Lublinsky for elucidating discussions on the

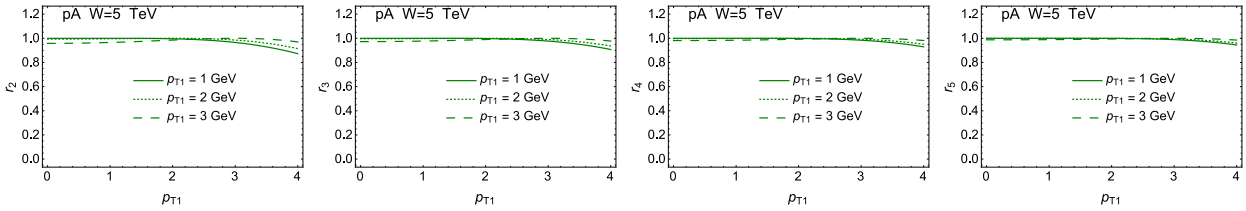

Fig. 21-a Fig. 21-b Fig. 21-c Fig. 21-d

FIG. 21: The ration r_n versus p_T at $W = 5\,TeV$ for proton-lead collisions.

subject of this paper. This research was supported by the BSF grant 2012124, by Proyecto Basal FB 0821(Chile) , Fondecyt (Chile) grant 1140842 and by CONICYT grant PIA ACT1406.

Appendix A

1. BFKL contribution for the interference diagram

In this appendix we derive the BFKL contribution to $\frac{d\sigma}{dy_1 d^2 p_{T1}}\left(k_T, |\boldsymbol{k_T} + \boldsymbol{p}_{T,12}|\right)$ given by Eq. (14).

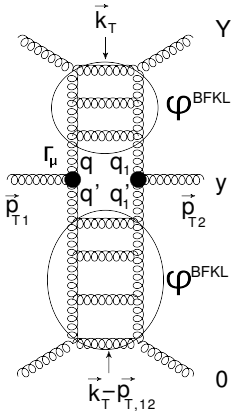

FIG. 22: The graphical representation of Eq. (14).

The Lipatov vertices $\Gamma_\mu\left(q_T, p_{T1}\right)$ and $\Gamma_\mu\left(q_{T1}, p_{T2}\right)$ have the form (see book [16] for example):

$$\Gamma_\mu\left(q_T, p_{T1}\right) \;=\; \frac{1}{p_{T1}^2}\left(q_T^2\,\boldsymbol{p}_{T1} \;-\; \boldsymbol{q}_T\,p_{T1}^2\right); \qquad \Gamma_\mu\left(q_{T1}, p_{T2}\right) \;=\; \frac{1}{p_{T2}^2}\left(q_{T1}^2\,\boldsymbol{p}_{T2} \;-\; \boldsymbol{q}_{T1}\,p_{T2}^2\right); \tag{A1}$$

and

$$\Gamma_\mu\left(q_T, p_{T1}\right)\,\Gamma_\mu\left(q_{T1}, p_{T2}\right) \;=\; \frac{q_{T1}^2\,\left(\boldsymbol{q}_T - \boldsymbol{p}_{T2}\right)^2}{p_{T2}^2} \;+\; \frac{q_T^2\,\left(\boldsymbol{q}_{T1} - \boldsymbol{p}_{T1}\right)^2}{p_{T1}^2} \;-\; k_T^2 \;-\; p_{T,12}^2\,\frac{q_T^2\,q_{T1}^2}{p_{T1}^2\,p_{T2}^2} \tag{A2}$$

where $\boldsymbol{p}_{T,12} \;=\; \boldsymbol{p}_{T1} - \boldsymbol{p}_{T2}$, $\boldsymbol{q}_T^{'} \;=\; \boldsymbol{q}_T - \boldsymbol{p}_{T1}$, $\boldsymbol{q}_{T1}^{'} \;=\; \boldsymbol{q}_{T1} - \boldsymbol{p}_{T2}$, and $\boldsymbol{q}_{T1} = \boldsymbol{q}_T - \boldsymbol{k}_T$. Eq. (A2) can be re-written as

$$\Gamma_\mu\left(q_T, p_{T1}\right)\,\Gamma_\mu\left(q_{T1}, p_{T2}\right) \;=\; \frac{q_{T1}^2\,\left(\boldsymbol{q}_T^{'} + \boldsymbol{p}_{T,12}\right)^2}{p_{T2}^2} \;+\; \frac{q_T^2\,\left(\boldsymbol{q}_{T1}^{'} - \boldsymbol{p}_{T,12}\right)^2}{p_{T1}^2} \;-\; k_T^2 \;-\; p_{T,12}^2\,\frac{q_T^2\,q_{T1}^2}{p_{T1}^2\,p_{T2}^2} \tag{A3}$$

$\phi^{\rm BFKL}$ satisfies the following equation:

$$\frac{\partial\phi^{\rm BFKL}\left(Y; q_T, k_T\right)}{\partial\,Y} \;=\; \bar{\alpha}_S\int\frac{d^2q_T'}{\pi}\,K\left(k_T, q_T'\right)\,\phi^{\rm BFKL}\left(Y; q_T', k_T\right) \tag{A4}$$

where

$$K\left(k_T, q_T^{\prime}\right) \;=\; \left(\frac{q_{T1}^2\, q_T^{\prime 2}}{p_T^2} \;+\; \frac{q_T^2\, q_{T1}^{\prime 2}}{p_T^2} \;-\; k_T^2\right) \frac{1}{q_T^{\prime 2}\, q_{T1}^{\prime 2}} \;-\; \left\{ q_T^2 \int \frac{d^2 p_T}{p_T^2\, \left(\boldsymbol{q}_T - \boldsymbol{p}_T\right)^2} \;+\; q_T^{\prime 2} \int \frac{d^2 p_T}{p_T^2\, \left(\boldsymbol{q}_T^{\prime} - \boldsymbol{p}_T\right)^2} \right\} \delta^{(2)}\left(\boldsymbol{q}_t^{\prime} - \boldsymbol{q}_T\right) \tag{A5}$$

Eq. (A4) is the BFKL equation in the momentum representation, which has the following form in the coordinate representation[21, 34]:

$$\frac{\partial N^{\mathrm{BFKL}}\left(Y; x_{12}, b\right)}{\partial\, Y} \;= \; \bar{\alpha}_S \int \frac{d^2 x_3}{\pi}\, \frac{x_{12}^2}{x_{13}^2\, x_{23}^2} \left\{ N\left(Y; x_{13}, \boldsymbol{b} - \frac{1}{2}\boldsymbol{x}_{23}\right) \;+\; N\left(Y; x_{23}, \boldsymbol{b} - \frac{1}{2}\boldsymbol{x}_{13}\right) \;-\; N\left(Y; x_{13}, b\right) \right\} \tag{A6}$$

where[16, 51]

$$\frac{1}{\left(\boldsymbol{q}_T + \frac{1}{2}\boldsymbol{k}_T\right)^2\, \left(\frac{1}{2}\boldsymbol{k}_T - \boldsymbol{q}_T\right)^2} \phi^{\mathrm{BFKL}}\left(q_T, k_T\right) \;=\; \frac{2\, C_F}{\bar{\alpha}_S (2\pi)^3} \int d^2 b\, d^2 x_{12}\, e^{i \boldsymbol{q}_T \cdot \boldsymbol{x}_{12} \,+\, i \boldsymbol{k}_T \cdot \boldsymbol{b}}\, N^{\mathrm{BFKL}}\left(Y; x_{12}, b\right) \tag{A7}$$

For diagrams Fig. 2- c and Fig. 2-d $\boldsymbol{p}_{12} = 0$ and plugging Eq. (A7) in Eq. (14) we obtain that

$$\begin{aligned} \frac{d\sigma}{dy_1 d^2 p_{T1}}\left(k_T, k_T\right) \;&=\; \left(\frac{2\, C_F}{\bar{\alpha}_S (2\pi)^3}\right)^2 \int d^2 x_{12}\, d^2 b\, d^2 b^{\prime}\, e^{i \boldsymbol{p}_{T1} \cdot \boldsymbol{x}_{12} \,+\, i \boldsymbol{k}_T \cdot \boldsymbol{b}} \\ \times \Bigg\{ \frac{1}{p_{T1}^2} \Bigg(& \left(\left(\frac{1}{2}\boldsymbol{\nabla}_b \;+\; \boldsymbol{\nabla}_{x_{12}} \right)^2 N^{\mathrm{BFKL}}\left(Y - y; x_{12}, \boldsymbol{b} - \boldsymbol{b}^{\prime}\right) \right) \left(\left(\frac{1}{2}\boldsymbol{\nabla}_{b^{\prime}} \;-\; \boldsymbol{\nabla}_{x_{12}} \right)^2 N^{\mathrm{BFKL}}\left(y; x_{12}, \boldsymbol{b}^{\prime}\right) \right) \\ + & \left(\left(\frac{1}{2}\boldsymbol{\nabla}_b \;-\; \boldsymbol{\nabla}_{x_{12}} \right)^2 N^{\mathrm{BFKL}}\left(Y - y; x_{12}, \boldsymbol{b} - \boldsymbol{b}^{\prime}\right) \right) \left(\left(\frac{1}{2}\boldsymbol{\nabla}_{b^{\prime}} \;+\; \boldsymbol{\nabla}_{x_{12}} \right)^2 N^{\mathrm{BFKL}}\left(y; x_{12}, \boldsymbol{b}^{\prime}\right) \right) \Bigg) \\ - & \left(\boldsymbol{\nabla}_b N^{\mathrm{BFKL}}\left(Y - y; x_{12}, \boldsymbol{b} - \boldsymbol{b}^{\prime}\right)\right) \cdot \left(\boldsymbol{\nabla}_{b^{\prime}} N^{\mathrm{BFKL}}\left(y; x_{12}, \boldsymbol{b}^{\prime}\right)\right) \Bigg\} \end{aligned} \tag{A8}$$

Eq. (A8) in the limit $k_T \to 0$, degenerates to the expression for the inclusive cross section which has the elegant form derived in Ref.[51]

$$\frac{d\sigma}{dy_1 d^2 p_{T1}}\left(k_T = 0, k_T = 0\right) \;= \; \left(\frac{2\, C_F}{\bar{\alpha}_S (2\pi)^3}\right)^2 \frac{1}{p_{T1}^2} \int d^2 x_{12}\, e^{i \boldsymbol{p}_{T1} \cdot x_{12}} \left(\nabla_{x_{12}}^2 \int d^2 b\, N^{\mathrm{BFKL}}\left(Y - y; x_{12}, \boldsymbol{b}\right) \right) \left(\nabla_{x_{12}}^2 \int d^2 b^{\prime}\, N^{\mathrm{BFKL}}\left(y; x_{12}, \boldsymbol{b}^{\prime}\right) \right) \tag{A9}$$

The interesting feature of Eq. (A8) and Eq. (A9) is, that they remain correct, if we replace $2N^{\mathrm{BFKL}}$ by $N_G = 2\,N \,-\, N^2$, where N is the solution of the Balitsky-Kovchegov equation[35]. Inside the saturation domain where $N \to 1$, both equations lead to negligible contributions. In other words, in both equations the main contributions stem from the vicinity of the saturation scale, where $x_{12}^2\, Q_s^2 \approx 1$.

The solution for the scattering amplitude of two dipoles r_1 and r_2 to Eq. (A6) is known[21]

$$N_{I\!P}\left(r_1, r_2; Y, b\right) \;= \; \sum_{n=0}^{\infty} \int \frac{d\gamma}{2\,\pi\, i}\, \phi_{in}^{(n)}(\gamma; r_2)\; d^2\, R_1\; d^2\, R_2\, \delta(\boldsymbol{R}_1 - \boldsymbol{R}_2 - \boldsymbol{b})\, e^{\omega(\gamma, n)\, Y}\, E^{\gamma, n}\left(r_1, R_1\right)\, E^{1-\gamma, n}\left(r_2, R_2\right) \tag{A10}$$

where the functions $\phi_{in}^{(n)}(\gamma; r_2)$ are determined by the initial conditions at low energies and

$$\omega(\gamma, n) \;=\; \bar{\alpha}_S \chi(\gamma, n) \;=\; \bar{\alpha}_S \left(2\psi\left(1\right) \;-\; \psi\left(\gamma + |n|/2\right) \;-\; \psi\left(1 - \gamma + |n|/2\right)\right); \tag{A11}$$

where $\psi(\gamma) = d\ln\Gamma(\gamma)/d\gamma$ and $\Gamma(\gamma)$ is Euler gamma function. Functions $E^{n,\gamma}(\rho_{1a},\rho_{2a})$ are given by the following equations.

$$E^{n,\gamma}(\rho_{1a},\rho_{2a}) = \left(\frac{\rho_{12}}{\rho_{1a}\,\rho_{2a}}\right)^{1-\gamma+n/2}\left(\frac{\rho^*_{12}}{\rho^*_{1a}\,\rho^*_{2a}}\right)^{1-\gamma-n/2}, \tag{A12}$$

In Eq. (A12) we use complex numbers to characterize the point on the plane

$$\rho_i = x_{i,1} + i\,x_{i,2}; \quad \rho^*_i = x_{i,1} - i\,x_{i,2} \tag{A13}$$

where the indices 1 and 2 denote two transverse axes. Note that

$$\rho_{12}\,\rho^*_{12} = r_i^2; \qquad \rho_{1a}\,\rho^*_{1a} = \left(\boldsymbol{R}_i - \frac{1}{2}\boldsymbol{r}_i\right)^2 \qquad \rho_{2a}\,\rho^*_{2a} = \left(\boldsymbol{R}_i + \frac{1}{2}\boldsymbol{r}_i\right)^2 \tag{A14}$$

At large values of Y, the main contribution stems from the first term with $n=0$. For this term, Eq. (A12) can be re-written in the form

$$E^{\gamma,0}(r_i,R_i) = \left(\frac{r_i^2}{(\boldsymbol{R}_i + \frac{1}{2}\boldsymbol{r}_i)^2\,(\boldsymbol{R}_i - \frac{1}{2}\boldsymbol{r}_i)^2}\right)^{1-\gamma}. \tag{A15}$$

The integrals over R_1 and R_2 were taken in Refs.[21, 59] and at $n=0$ we have

$$H^\gamma(w,w^*) \equiv \int d^2R_1\,E^{\gamma,0}(r_1,R_1)\,E^{1-\gamma,0}(r_2,\boldsymbol{R}_1-\boldsymbol{b}) = \tag{A16}$$

$$\frac{(\gamma-\frac{1}{2})^2}{(\gamma(1-\gamma))^2}\Big\{b_\gamma\,w^\gamma\,w^{*\gamma}\,F(\gamma,\gamma,2\gamma,w)\;F(\gamma,\gamma,2\gamma,w^*)$$

$$+b_{1-\gamma}w^{1-\gamma}w^{*1-\gamma}F(1-\gamma,1-\gamma,2-2\gamma,w)\;F(1-\gamma,1-\gamma,2-2\gamma,w^*)\Big\}$$

$$\xrightarrow{b\gg r_1 \text{ and/or } r_2} \frac{(\gamma-\frac{1}{2})^2}{(\gamma(1-\gamma))^2}\Big\{b_\gamma\,w^\gamma\,w^{*\gamma} + b_{1-\gamma}w^{1-\gamma}w^{*1-\gamma}\Big\} = \frac{(\gamma-\frac{1}{2})^2}{(\gamma(1-\gamma))^2}\Big\{b_\gamma\left(\frac{r_1^2\,r_2^2}{b^4}\right)^\gamma + b_{1-\gamma}\left(\frac{r_1^2\,r_2^2}{b^4}\right)^{1-\gamma}\Big\}$$

where F is hypergeometric function [60]. In Eq. (A16) $w\,w^*$ and b_γ are equal

$$w\,w^* = \frac{r_1^2\,r_2^2}{\left(\boldsymbol{b}-\frac{1}{2}(\boldsymbol{r}_1-\boldsymbol{r}_2)\right)^2\left(\boldsymbol{b}+\frac{1}{2}(\boldsymbol{r}_1-\boldsymbol{r}_2)\right)^2}; \qquad b_\gamma = \pi^3\,2^{4(1/2-\gamma)}\,\frac{\Gamma(\gamma)}{\Gamma(1/2-\gamma)}\,\frac{\Gamma(1-\gamma)}{\Gamma(1/2+\gamma)}. \tag{A17}$$

Therefore, at large b, $N^{\rm BFKL}$ decreases as a power of b which violates the Froissart theorem [14]. At present, as has been mentioned above, we cannot suggest a modification of the equation of the CGC/saturation approach in which the correct[23] exponential behaviour at large b would be incorporated. So we doomed to build a model. We discussed our model in section 3.

2. Born diagrams

The spirited discussions with our colleagues, showed us that it would be benificial to add a general discussion of the BFKL contribution, by calculating of the first Born diagrams for the production of two identical gluons that have rapidities y_1 and y_2, and carry momenta $\boldsymbol{p}_{T1}$ and $\boldsymbol{p}_{T2}$. These diagrams are shown in Fig. 23 for the scattering of the bound states of two oniums (two dipoles). Such a model for the scattering systems allows us to use the perturbative QCD approach, and has the analogy in the simplest bound system: deuteron.

The two onium bound state is described by the wave function $\Psi(\boldsymbol{R}_1-\boldsymbol{R}_2)$, where R_i is the coordinate of the onium which is equal $\boldsymbol{R}_i = \frac{1}{2}(\boldsymbol{x}_i+\boldsymbol{y}_i)$ where $\boldsymbol{x}_i$ and $\boldsymbol{y}_i$ are coordinates of quark and antiquark in the onium (see Fig. 23). We introduce two new functions that describe the form factor of our bound state ($G(q)$), and the interaction of two gluons with the onium:

$$G(q) = \int d^2R\,|\Psi(R)|^2\,e^{i\,\boldsymbol{q}\cdot\boldsymbol{R}} \quad \text{with} \quad \boldsymbol{R}=\boldsymbol{R}_1-\boldsymbol{R}_2;$$

$$\phi_{\rm onium}(q,k) = 2\int d^2r_i\,|\psi_{\rm onium}(r_i)|^2\,e^{i\,\frac{1}{2}\boldsymbol{k}\cdot\boldsymbol{r}_i}\left(1+e^{i\boldsymbol{q}\cdot\boldsymbol{r}_i}\right) \qquad \text{with} \qquad \boldsymbol{r}_i = \boldsymbol{x}_i - \boldsymbol{y}_i; \tag{A18}$$

The contribution of the diagram of Fig. 23 can be written as[2]

$$\sigma_{\rm interference} \,\propto\, \int \frac{d^2k}{4\pi^2}\, G\left(k\right)\, G\left(\boldsymbol{k}+\boldsymbol{p}_{T,12}\right)\, I^2\left(\boldsymbol{k},\boldsymbol{p}_{T1},\boldsymbol{p}_{T2}\right) \tag{A19}$$

where

$$\begin{aligned} I\left(\boldsymbol{k},\boldsymbol{p}_{T1},\boldsymbol{p}_{T2}\right) \;&\propto\; \int \frac{d^2q}{4\,\pi^2}\, \phi_{\rm onium}\left(\boldsymbol{k},\boldsymbol{q}\right)\, \phi_{\rm onium}\left(\boldsymbol{k}\,-\,\boldsymbol{p}_{T,12},\boldsymbol{q}\right) \\ &\times\; \left\{ \frac{1}{q^2\,\left(\boldsymbol{k}-\boldsymbol{q}\right)^2}\, \Gamma_\mu\left(q_T,p_{T1}\right)\, \Gamma_\mu\left(q_{T1},p_{T2}\right)\; \frac{1}{\left(\boldsymbol{q}-\boldsymbol{p}_{T1}\right)^2\,\left(\boldsymbol{k}-\boldsymbol{p}_{T,12}-\boldsymbol{q}\right)^2} \right\} \end{aligned} \tag{A20}$$

where $\Gamma_\mu\left(q_T,p_{T1}\right)\,\Gamma_\mu\left(q_{T1},p_{T2}\right)$ is given by Eq. (A2) and Eq. (A3).

One can see from Eq. (A19) and Eq. (3) that the typical $q \approx 1/r$, where r is he size of the onium , while the typical values of $k \propto 1/R$, where R is the size of the bound state. Assuming that $R \gg r$, we see that $k \ll q$. Anticipating $p_{T,12} \propto 1/R$, we can reduce the contribution of the interference diagram to the following form:

$$\sigma_{\rm interference} \,\propto\, \frac{1}{p_{T1}^2\,p_{T,2}^2} \int \frac{d^2k}{4\pi^2}\, G\left(k\right)\, G\left(\boldsymbol{k}+\boldsymbol{p}_{T,12}\right) \left(\int \frac{d^2q}{4\pi^2} \frac{1}{q^2\,\left(\boldsymbol{q}-\boldsymbol{p}_{T1}\right)^2} \right)^2 \tag{A21}$$

In Eq. (A21) we assume that $p_{T1} \approx p_{T2}$ and one can see that $p_{T,12}$ from this equation is indeed of the order of $1/R$, being much smaller than p_{Ti} if they are of the order of $1/r$. For $1/R \ll p_{Ti} \ll 1/r$ we need to take $\Gamma_\mu\left(q_T,p_{T1}\right)\,\Gamma_\mu\left(q_{T1},p_{T2}\right) \,=\, \left(\frac{1}{p_{T1}^2}\,+\,\frac{1}{p_{T2}^2}\right)\,\frac{1}{q^4}$.

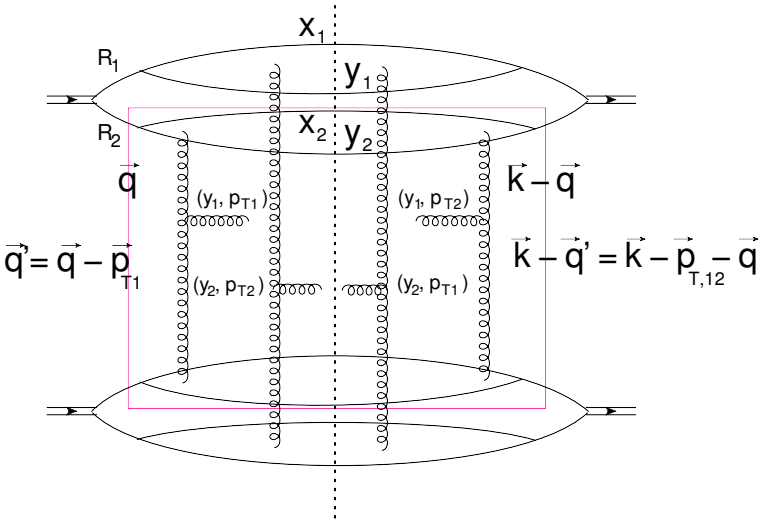

FIG. 23: The Born interference diagram for production of two identical gluons with rapidities:y_1 and y_2 and transverse momenta $\boldsymbol{p}_{T1}$ and $\boldsymbol{p}_{T2}$.$\boldsymbol{R}_i = \frac{1}{2}\left(\boldsymbol{x}_i+\boldsymbol{y}_i\right)$, $\boldsymbol{p}_{T,12}=\boldsymbol{p}_{T1}-\boldsymbol{p}_{T2}$. Red rectangle shows function $\Phi\left(\boldsymbol{k},\boldsymbol{p}_{T1},\boldsymbol{p}_{T2}\right)$(see text).

Appendix B: BE correlations in the model: diffractive production in the small mass region.

a. Inclusive production

The inclusive production in the framework of the CGC/saturation approach comprises two stages: the gluon mini-jet productions and the decay of this mini-jet into hadrons. For mini-jet production, we use the k_T factorization

[2] We omit all numerical factors as well as $\bar{\alpha}_S^6$.

formula, which has been proven in Ref. [51] in the framework of the CGC/saturation approach (see appendix for details).

$$\frac{d\sigma}{dy\,d^2p_T} \;=\; \frac{2\pi\bar{\alpha}_S}{C_F}\frac{1}{p_T^2}\int d^2k_T\;\phi_G^{h_1}\left(x_1;\boldsymbol{k}_T\right)\phi_G^{h_2}\left(x_2;\boldsymbol{p}_T-\boldsymbol{k}_T\right) \tag{B1}$$

where $\phi_G^{h_i}$ denotes the probability to find a gluon that carries the fraction x_i of energy with k_T transverse momentum, and $\bar{\alpha}_S = \alpha_S N_c/\pi$, with the number of colours equal to N_c. $\frac{1}{2}Y + y = \ln(1/x_1)$ and $\frac{1}{2}Y - y = \ln(1/x_2)$. $\phi_G^{h_i}$ is the solution of the Balitsky-Kovchegov(BK) [35] non-linear evolution equation, and can be viewed as the sum of 'fan' diagrams of the BFKL Pomeron interactions, shown in Fig. 24.

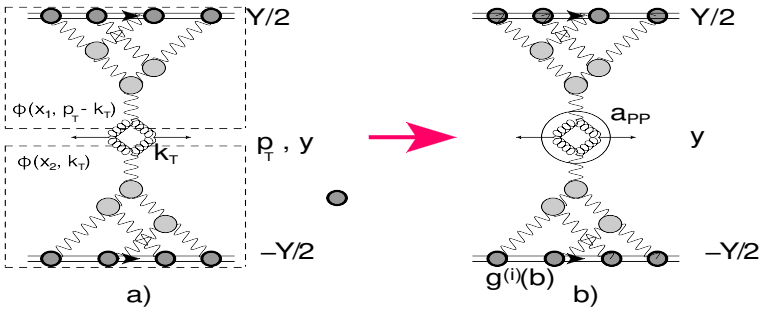

FIG. 24: The graphic representation of Eq. (B1) (see Fig. 24-a).For the sake of simplicity all other indices in $\phi\left(x_1, p_T - k_T\right)$ and $\phi\left(x_2, k_T\right)$ are omitted. The wavy lines denote the BFKL Pomerons, while the helical lines illustrate the gluons. In Fig. 24-b the Mueller diagram for inclusive production is shown.

In our model the sum of 'fan' diagrams is given by Eq. (29). Assuming that the main contribution to

$$\frac{d\sigma}{dy} \;=\; \int d^2p_T\,\frac{d\sigma}{dy\,d^2p_T}$$

stems from $p_T \leq Q_s$, we obtain the following formula:

$$\begin{aligned}\frac{d\sigma}{dy} \;&=\; \int d^2p_T\,\frac{d\sigma}{dy\,d^2p_T} \;=\; a_{I\!P I\!P}\,\ln\left(W/W_0\right)\left(\alpha^2\,In^{(1)}\left(\frac{1}{2}Y+y\right)+\beta^2\,In^{(2)}\left(\frac{1}{2}Y+y\right)\right)\\ &\times\left(\alpha^2\,In^{(1)}\left(\frac{1}{2}Y-y\right)+\beta^2\,In^{(2)}\left(\frac{1}{2}Y-y\right)\right)\end{aligned} \tag{B2}$$

where

$$\begin{aligned}&In^{(i)}\left(y\right) \;=\; \int d^2b\;N^{BK}\left(g^{(i)}\,S\left(m_i,b\right)\,\tilde{G}_{I\!P}\left(y\right)\right)\qquad\text{or}\qquad In^{(i)}\left(y\right)=I_i^{\rm BK}\left(y,Q_T=0\right);\\ &\text{with}\quad I_i^{\rm BK}\left(y,Q_T\right) \;=\; \int d^2b\,e^{i\boldsymbol{b}\cdot\boldsymbol{Q}_T}\;N^{BK}\left(g^{(i)}\,S\left(m_i,b\right)\,\tilde{G}_{I\!P}\left(y\right)\right)\end{aligned} \tag{B3}$$

where $\tilde{G}_{I\!P}\left(y\right)$ and N^{BK} have been defined in Eq. (46) and in Eq. (29), respectively. Regarding the factor in front of Eq. (B2) i.e. $\ln\left(W/W_0\right)$, where $W=\sqrt{s}$ is the energy of collision in c.m. frame, and W_0 is the value of energy from which we start our approach. One can see that Eq. (B1) is divergent in the region of small $p_T < Q_s$. Indeed, in this region ϕ's in Eq. (B1) do not depend on p_T, since $k_T \approx Q_s > p_T$, and the integration over p_T leads to $\ln\left(Q_s^2/m_{soft}^2\right)$, where m_{soft} is the non-perturbative scale, that includes the confinement of quarks and gluons ($m_{soft}\sim\Lambda_{QCD}$).

b. LRR correlations

In our previous paper [28], we showed that in the framework of our model that has been described above, the main source of the long range rapidity correlation, is the correlation between two parton showers. In other words, it was

shown that the contribution to the correlation function from enhanced and semi-enhanced diagrams, turns out to be negligibly small.

The appropriate Mueller diagrams are shown in Fig. 25. Examining this diagram, we see that the contribution to the double inclusive cross section, differs from the product of two single inclusive cross sections. This difference generates the rapidity correlation function, which is defined as

$$R\left(y_1,y_2\right) \;=\; \frac{\frac{1}{\sigma_{in}}\frac{d^2\sigma}{dy_1\,dy_2}}{\frac{1}{\sigma_{in}}\frac{d\sigma}{dy_1}\,\frac{1}{\sigma_{in}}\frac{d\sigma}{dy_2}} \;-\; 1 \tag{B4}$$

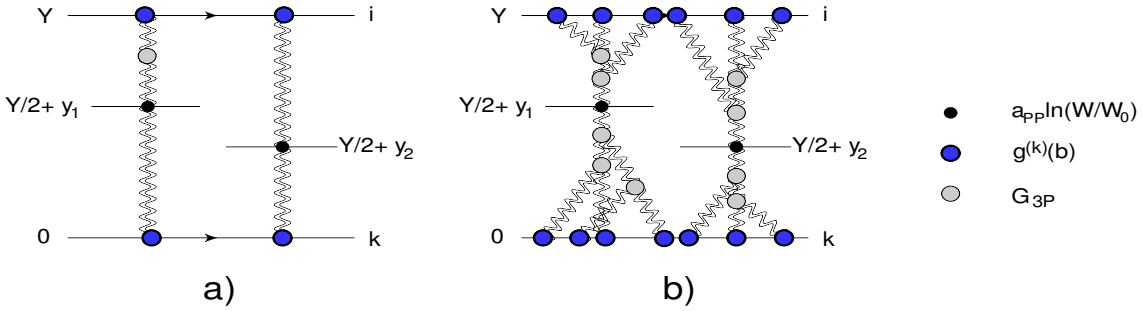

FIG. 25: The Mueller diagram for the rapidity correlation between two particles produced in two parton showers. Fig. 25-a shows the first Mueller diagram, while Fig. 25-b indicates the structure of general diagrams. The double wavy lines describe the dressed BFKL Pomerons. The blobs stand for the vertices as shown in the legend.

There are two reasons for the difference between the double inclusive cross section due to production of two parton showers, and the products of inclusive cross sections: the first, is that in the expression for the double inclusive cross section, we integrate the product of the single inclusive inclusive cross sections, over b or Q_T(see Fig. 24-a and Eq. (13)). The second, is that the summation over i and k for the product of single inclusive cross sections, is for fixed i and k(see Fig. 24-a).

Introducing the following new function, enables us to write the analytical expression for the double inclusive cross section:

$$\begin{aligned} I^{(i,k)}\left(y,b\right) \;&=\; \tilde{a}_{I\!P I\!P}\int d^2b'\; N^{BK}\left(g^{(i)}\,S\left(m_i,b'\right)\tilde{G}^{\rm dressed}\left(r_\perp=1/m,\frac{1}{2}Y+y\right)\right) \\ &\times\; N^{BK}\left(g^{(k)}\,S\left(m_k,\boldsymbol{b}-\boldsymbol{b}'\right)\tilde{G}^{\rm dressed}\left(r_\perp=1/m,\frac{1}{2}Y-y\right)\right) \end{aligned} \tag{B5}$$

where $\tilde{a}_{I\!P I\!P}=a_{I\!P I\!P}\,\ln\left(W/W_0\right)$.

Using Eq. (B5) we can write the double inclusive cross section in two equivalent forms

$$\begin{aligned} \frac{d^2\sigma^{\text{2 parton showers}}}{dy_1\;dy_2} \;&=\; \int d^2p_{1T}\,d^2p_{2T}\,\frac{d^2\sigma^{\text{2 parton showers}}}{dy_1\;dy_2\,d^2p_{1T}\,d^2p_{2T}} \;=\; \int d^2b\,\Big\{\alpha^4\,I^{(1,1)}\left(y_1,b\right)\,I^{(1,1)}\left(y_2,b\right) \\ &+\alpha^2\,\beta^2\,\Big(I^{(1,2)}\left(y_1,b\right)\,I^{(1,2)}\left(y_2,b\right)\;+\;I^{(2,1)}\left(y_1,b\right)\,I^{(2,1)}\left(y_2,b\right)\Big)\;+\;\beta^4\,I^{(2,2)}\left(y_1,b\right)\,I^{(2,2)}\left(y_2,b\right)\Big\} \end{aligned} \tag{B6}$$

$$\begin{aligned} &= \frac{\tilde{a}^2_{I\!P I\!P}}{p^2_{T1}\,p^2_{T2}}\int d^2Q_T\Big(\alpha^2 I^{\rm BK}_1\left(\frac{1}{2}Y+y_1;Q_T\right)I^{\rm BK}_1\left(\frac{1}{2}Y+y_2;Q_T\right)\;+\;\beta^2\,I^{\rm BK}_2\left(\frac{1}{2}Y+y_1;Q_T\right)I^{\rm BK}_2\left(\frac{1}{2}Y+y_2;Q_T\right)\Big) \\ &\times\Big(\alpha^2 I^{\rm BK}_1\left(\frac{1}{2}Y-y_1;Q_T\right)I^{\rm BK}_1\left(\frac{1}{2}Y-y_2;Q_T\right)\;+\;\beta^2\,I^{\rm BK}_2\left(\frac{1}{2}Y-y_1;Q_T\right)I^{\rm BK}_2\left(\frac{1}{2}Y-y_2;Q_T\right)\Big) \\ &\equiv\; \frac{\tilde{a}^2_{I\!P I\!P}}{p^2_{T1}\,p^2_{T2}}\int d^2Q_T\,F^{\rm BK}_{12}\left(\frac{1}{2}Y+y_1,\frac{1}{2}Y+y_2;Q_T\right)\;F^{\rm BK}_{12}\left(\frac{1}{2}Y-y_1,\frac{1}{2}Y-y_2;Q_T\right) \end{aligned} \tag{B7}$$

where $F^{\rm BK}_{12}$ is equal to

$$F_{12}^{\rm BK}\left(Y_1,Y_2;Q_T\right)\,=\,\alpha^2 I_1^{\rm BK}\left(Y_1;Q_T\right)I_1^{\rm BK}\left(Y_2;Q_T\right)\,+\,\beta^2\,I_2^{\rm BK}\left(Y_1;Q_T\right)I_2^{\rm BK}\left(Y_2;Q_T\right) \tag{B8}$$

Recall that all rapidities are in the c.m. frame.

c. v_n for proton-proton collisions

Using Eq. (B7), Eq. (10) can be re-written in the following form

$$\begin{aligned}\frac{d^2\sigma}{dy_1\,dy_2 d^2p_{T1}d^2p_{T2}}\,&=\,\frac{\tilde{a}^2_{I\!P\,I\!P}}{p^2_{T1}\,p^2_{T2}}\int d^2k_T\,F_{12}^{\rm BK}\left(\frac{1}{2}Y+y_1,\frac{1}{2}Y+y_2;k_T\right)\,F_{12}^{\rm BK}\left(\frac{1}{2}Y-y_1,\frac{1}{2}Y-y_2;k_T\right)\\&+\,\frac{\tilde{a}^2_{I\!P\,I\!P}}{N_c^2-1}\,\frac{1}{4}\left(\frac{1}{p^2_{T1}}\,+\,\frac{1}{p^2_{T2}}\right)^2\int d^2k_T\,F_{12}^{\rm BK}\left(\frac{1}{2}Y+y_1,\frac{1}{2}Y+y_2;\boldsymbol{k}_T\right)\,F_{12}^{\rm BK}\left(\frac{1}{2}Y-y_1,\frac{1}{2}Y-y_2;\boldsymbol{k}_T+\boldsymbol{p}_{T,12}\right)\end{aligned} \tag{B9}$$

In Eq. (B9) we neglected the contribution $\propto p^2_{T,12}$ in the vertex of gluon emission in Fig. 22 (see Appendix A1), as well as the dependence of the BFKL Pomeron on the momentum transfer. The small size of both quantities stem from the fact that in our model, k_T dependence in Eq. (B9) is determined by the proton structure and the typical $k_T\sim m_1$ or m_2 (see Table 1), while typical transverse momentum in the BFKL Pomeron is about Q_s or m, and it is much larger than m_1 or m_2.

Appendix C: Hadron-nucleus interaction in the model

In the case of the hadron-nucleus interaction the general formula of Eq. (B7) can be re-written in the form[52]

$$\frac{d^2\sigma^{\text{2 parton showers}}}{dy_1\;dy_2}\,=\,\int d^2p_{1T}\,d^2p_{2T}\frac{d^2\sigma^{\text{2 parton showers}}}{dy_1\;dy_2\,d^2p_{1T}\,d^2p_{2T}}\,= \tag{C1}$$

$$\begin{aligned}&=\frac{\tilde{a}^2_{I\!P\,I\!P}}{p^2_{T1}\,p^2_{T2}}\int d^2Q_T\Bigg(\alpha^2 I_1^{\rm BK}\left(\frac{1}{2}Y+y_1;Q_T\right)I_1^{\rm BK}\left(\frac{1}{2}Y+y_2;Q_T\right)\,+\,\beta^2\,I_2^{\rm BK}\left(\frac{1}{2}Y+y_1;Q_T\right)I_2^{\rm BK}\left(\frac{1}{2}Y+y_2;Q_T\right)\Bigg)\\&\times I_A^{\rm BK}\left(\frac{1}{2}Y-y_1;Q_T\right)\,I_A^{\rm BK}\left(\frac{1}{2}Y-y_2;Q_T\right)\\&\equiv\;\frac{\tilde{a}^2_{I\!P\,I\!P}}{p^2_{T1}\,p^2_{T2}}\int d^2Q_T\,F_{12}^{\rm BK}\left(\frac{1}{2}Y+y_1,\frac{1}{2}Y+y_2;Q_T\right)\,F_A^{\rm BK}\left(\frac{1}{2}Y-y_1,\frac{1}{2}Y-y_2;Q_T\right)\end{aligned} \tag{C2}$$

where

$$I_A^{\rm BK}\left(y,Q_T\right)\,=\,\int d^2b e^{i\boldsymbol{b}\cdot\boldsymbol{Q}_T}\,N^{\rm BK}\left(\left(\alpha^2 In^{(1)}\left(y\right)\,+\,\beta^2\,In^{(2)}\left(y\right)\right)S_A\left(b\right)\right) \tag{C3}$$

where $In^{(i)}$ are defined in Eq. (B3) and $S_A\left(b\right)$ is the nucleus Wood-Saxon distribution[53] given by

$$S_A\left(b\right)\,=\,\int_{-\infty}^{\infty}dz\,\frac{\rho_0}{1\,+\,\exp\left(\frac{\sqrt{z^2+b^2}-R_A}{h}\right)}\qquad\text{where}\qquad\int d^2b\,S_A\left(b\right)\,=\,A \tag{C4}$$

For gold we have $R_A=6.38\,fm$ and $h=0.535\,fm$, while for lead we have $R_A=6.68\,fm$ and $h=0.546\,fm$ [53]. In Eq. (C2) we have taken into account that the typical impact parameters in hadron-hadron interaction are much smaller than the radius of nucleus (R_A). Indeed, the typical b in hadron-hadron collisions are $\alpha'_{eff}Y$ or less, where α'_{eff} is the effective slope of the BFKL Pomeron trajectory, which occurs in our model as a result of shadowing corrections.

Using Eq. (C2) we can re-write Eq. (B9) for proton-proton in the following form for proton-nucleus scattering

$$\begin{aligned}\frac{d^2\sigma}{dy_1\,dy_2 d^2p_{T1}d^2p_{T2}}\,&=\,\frac{\tilde{a}^2_{I\!P\,I\!P}}{p^2_{T1}\,p^2_{T2}}\int d^2k_T\,F_{12}^{\rm BK}\left(\frac{1}{2}Y+y_1,\frac{1}{2}Y+y_2;k_T\right)\,F_A^{\rm BK}\left(\frac{1}{2}Y-y_1,\frac{1}{2}Y-y_2;k_T\right)\\&+\,\frac{\tilde{a}^2_{I\!P\,I\!P}}{N_c^2-1}\,\frac{1}{4}\left(\frac{1}{p^2_{T1}}\,+\,\frac{1}{p^2_{T2}}\right)^2\int d^2k_T\,F_{12}^{\rm BK}\left(\frac{1}{2}Y+y_1,\frac{1}{2}Y+y_2;\boldsymbol{k}_T+\boldsymbol{p}_{T,12}\right)\,F_A^{\rm BK}\left(\frac{1}{2}Y-y_1,\frac{1}{2}Y-y_2;\boldsymbol{k}_T\right)\end{aligned} \tag{C5}$$

and for nucleus-nuclues scattering we have

$$\frac{d^2\sigma}{dy_1\,dy_2 d^2p_{T1}d^2p_{T2}} = \frac{\tilde{a}^2_{I\!P I\!P}}{p^2_{T1}\,p^2_{T2}}\int d^2k_T\,F^{\rm BK}_{12}\left(\frac{1}{2}Y+y_1,\frac{1}{2}Y+y_2;k_T\right)\,F^{\rm BK}_{A}\left(\frac{1}{2}Y-y_1,\frac{1}{2}Y-y_2;k_T\right) \tag{C6}$$
$$+\frac{\tilde{a}^2_{I\!P I\!P}}{N^2_c-1}\,\frac{1}{4}\left(\frac{1}{p^2_{T1}}+\frac{1}{p^2_{T2}}\right)^2\int d^2k_T\,F^{\rm BK}_{A}\left(\frac{1}{2}Y+y_1,\frac{1}{2}Y+y_2;\boldsymbol{k}_T+\boldsymbol{p}_{T,12}\right)\,F^{\rm BK}_{A}\left(\frac{1}{2}Y-y_1,\frac{1}{2}Y-y_2;\boldsymbol{k}_T\right)$$

* Electronic address: gotsman@post.tau.ac.il
† Electronic address: leving@post.tau.ac.il, eugeny.levin@usm.cl
‡ Electronic address: maor@post.tau.ac.il

[1] E. Gotsman, E. Levin and U. Maor, arXiv:1604.04461 [hep-ph].
[2] V. Khachatryan *et al.* [CMS Collaboration], arXiv:1510.03068 [nucl-ex]; JHEP **1009** (2010) 091 [arXiv:1009.4122 [hep-ex]]. arXiv:1510.03068 [nucl-ex].
[3] J. Adams *et al.* [STAR Collaboration], Phys. Rev. Lett. **95** (2005) 152301 [nucl-ex/0501016].
[4] B. Alver *et al.* [PHOBOS Collaboration], Phys. Rev. Lett. **104** (2010) 062301 [arXiv:0903.2811 [nucl-ex]].
[5] H. Agakishiev *et al.* [STAR Collaboration], arXiv:1010.0690 [nucl-ex].
[6] S. Chatrchyan *et al.* [CMS Collaboration], Phys. Lett. B **718** (2013) 795 [arXiv:1210.5482 [nucl-ex]]; V. Khachatryan *et al.* [CMS Collaboration], JHEP **1009** (2010) 091, [arXiv:1009.4122 [hep-ex]].
[7] S. Chatrchyan *et al.* [CMS Collaboration], JHEP **1402** (2014) 088, [arXiv:1312.1845 [nucl-ex]]; Phys. Rev. C **89** (2014) no.4, 044906; [arXiv:1310.8651 [nucl-ex]]; "Centrality dependence of dihadron correlations and azimuthal anisotropy harmonics in PbPb collisions at $\sqrt{s_{NN}} = 2.76$ TeV," Eur. Phys. J. C **72** (2012) 2012 [arXiv:1201.3158 [nucl-ex]]; JHEP **1402** (2014) 088 doi:10.1007/JHEP02(2014)088 [arXiv:1312.1845 [nucl-ex]].
[8] J. Adam *et al.* [ALICE Collaboration], arXiv:1604.07663 [nucl-ex]; Phys. Rev. Lett. **116** (2016) no.13, 132302 doi:10.1103/PhysRevLett.116.132302 [arXiv:1602.01119 [nucl-ex]]; L. Milano [ALICE Collaboration], Nucl. Phys. A **931** (2014) 1017, [arXiv:1407.5808 [hep-ex]]; Y. Zhou [ALICE Collaboration], J. Phys. Conf. Ser. **509** (2014) 012029, [arXiv:1309.3237 [nucl-ex]].
[9] B. B. Abelev *et al.* [ALICE Collaboration], Phys. Rev. C **90** (2014) no.5, 054901, [arXiv:1406.2474 [nucl-ex]]; B. B. Abelev *et al.* [ALICE Collaboration], Phys. Lett. B **726** (2013) 164 doi:10.1016/j.physletb.2013.08.024 [arXiv:1307.3237 [nucl-ex]]; B. Abelev *et al.* [ALICE Collaboration], Phys. Lett. B **719** (2013) 29, [arXiv:1212.2001 [nucl-ex]].
[10] G. Aad *et al.* [ATLAS Collaboration], Phys. Rev. Lett. **116** (2016) 172301, [arXiv:1509.04776 [hep-ex]].
[11] G. Aad *et al.* [ATLAS Collaboration], Phys. Rev. C **90** (2014) no.4, 044906; [arXiv:1409.1792 [hep-ex]]; B. Wosiek [ATLAS Collaboration], Annals Phys. **352** (2015) 117; G. Aad *et al.* [ATLAS Collaboration], Phys. Lett. B **725** (2013) 60, [arXiv:1303.2084 [hep-ex]].
[12] B. Wosiek [ATLAS Collaboration], Phys. Rev. C **86** (2012) 014907, [arXiv:1203.3087 [hep-ex]].
[13] E. M. Levin, M. G. Ryskin and S. I. Troian, Sov. J. Nucl. Phys. **23** (1976) 222 [Yad. Fiz. **23** (1976) 423];
A. Capella, A. Krzywicki and E. M. Levin, Phys. Rev. D **44** (1991) 704.
[14] Y. V. Kovchegov and D. E. Wertepny, Nucl. Phys. A **906** (2013) 50, [arXiv:1212.1195 [hep-ph]];
[15] T. Altinoluk, N. Armesto, G. Beuf, A. Kovner and M. Lublinsky, Phys. Lett. B **752** (2016) 113, [arXiv:1509.03223 [hep-ph]]; T. Altinoluk, N. Armesto, G. Beuf, A. Kovner and M. Lublinsky, Phys. Lett. B **751** (2015) 448, [arXiv:1503.07126 [hep-ph]].
[16] Yuri V Kovchegov and Eugene Levin, *" Quantum Choromodynamics at High Energies"*, Cambridge Monographs on Particle Physics, Nuclear Physics and Cosmology, Cambridge University Press, 2012 .
[17] R. Hanbury Brown and R. Q. Twiss, Nature **178** (1956) 1046.
[18] G. Goldhaber, W. B. Fowler, S. Goldhaber and T. F. Hoang, Phys. Rev. Lett. **3**, 181 (1959); G. I. Kopylov and M. I. Podgoretsky, Sov. J. Nucl. Phys. **15**, 219 (1972) [Yad. Fiz. **15**, 392 (1972)]; G. Alexander, Rept. Prog. Phys. **66** (2003) 481, [hep-ph/0302130].
[19] A. H. Mueller, *Phys. Rev.* **D2** (1970) 2963.
[20] E. A. Kuraev, L. N. Lipatov, and F. S. Fadin, *Sov. Phys. JETP* **45**, 199 (1977); Ya. Ya. Balitsky and L. N. Lipatov, *Sov. J. Nucl. Phys.* **28**, 22 (1978).
[21] L. N. Lipatov, Phys. Rep. **286** (1997) 131; Sov. Phys. JETP **63** (1986) 904 and references therein.
[22] F. Ferro [TOTEM Collaboration], AIP Conf. Proc. **1350**, 172 (2011) ; G. Antchev *et al.* [TOTEM Collaboration], Europhys. Lett. **96**, 21002 (2011), **95**, 41001 (2011) [arXiv:1110.1385 [hep-ex]]; G. Antchev *et al.* [TOTEM Collaboration], Phys. Rev. Lett. **111** (2013) 26, 262001 [arXiv:1308.6722 [hep-ex]].
[23] M. Froissart, *Phys. Rev.* **123** (1961) 1053;
A. Martin, *"Scattering Theory: Unitarity, Analitysity and Crossing."* Lecture Notes in Physics, Springer-Verlag, Berlin-Heidelberg-New-York, 1969.
[24] A. Kovner and U. A. Wiedemann, Phys. Rev. D **66**, 051502, 034031 (2002) [hep-ph/0112140,hep-ph/0204277]; Phys. Lett. B **551**, 311 (2003) [hep-ph/0207335].
[25] E. Gotsman, E. Levin and U. Maor, Eur. Phys. J. C **75** (2015) 5, 179 [arXiv:1502.05202 [hep-ph]].

[26] E. Gotsman, E. Levin and U. Maor, Eur. Phys. J. C **75** (2015) 1, 18 [arXiv:1408.3811 [hep-ph]].

[27] E. Gotsman, E. Levin and U. Maor, Phys. Lett. B **746** (2015) 154 [arXiv:1503.04294 [hep-ph]].

[28] E. Gotsman, E. Levin and U. Maor, Eur. Phys. J. C **75** (2015) 11, 518 [arXiv:1508.04236 [hep-ph]].

[29] A. B. Kaidalov, Surveys High Energ. Phys. **13** (1999) 265; hep-ph/9710546, A. Capella, U. Sukhatme, C. I. Tan and J. Tran Thanh Van, Phys. Rept. **236** (1994) 225; A. B. Kaidalov, Phys. Rept. **50** (1979) 157.

[30] S. Gavin, L. McLerran and G. Moschelli, Phys. Rev. C **79** (2009) 051902, [arXiv:0806.4718 [nucl-th]]; N. Armesto, M. A. Braun and C. Pajares, Phys. Rev. C **75** (2007) 054902, [hep-ph/0702216]; K. Dusling, F. Gelis, T. Lappi and R. Venugopalan, Nucl. Phys. A **836** (2010) 159, [arXiv:0911.2720 [hep-ph]]; A. Dumitru, K. Dusling, F. Gelis, J. Jalilian-Marian, T. Lappi and R. Venugopalan, Phys. Lett. B **697** (2011) 21, [arXiv:1009.5295 [hep-ph]]; A. Kovner and M. Lublinsky, Phys. Rev. D **83** (2011) 034017, [arXiv:1012.3398 [hep-ph]]; F. Gelis, T. Lappi and R. Venugopalan, Phys. Rev. D **79** (2009) 094017 [arXiv:0810.4829 [hep-ph]].

[31] E. Levin and A. H. Rezaeian, Phys. Rev. D **84** (2011) 034031, [arXiv:1105.3275 [hep-ph]].

[32] A. Kovner and M. Lublinsky, Int. J. Mod. Phys. E **22** (2013) 1330001 [arXiv:1211.1928 [hep-ph]].

[33] L. McLerran and R. Venugopalan, Phys. Rev. **D49** (1994) 2233, 3352; **D50** (1994) 2225; **D53** (1996) 458; **D59** (1999) 09400.

[34] A. H. Mueller, Nucl. Phys. B **415**, 373 (1994); Nucl. Phys. B **437** (1995) 107 [arXiv:hep-ph/9408245].

[35] I. Balitsky, [arXiv:hep-ph/9509348]; *Phys. Rev.* **D60**, 014020 (1999) [arXiv:hep-ph/9812311]; Y. V. Kovchegov, *Phys. Rev.* **D60**, 034008 (1999), [arXiv:hep-ph/9901281].

[36] J. Jalilian-Marian, A. Kovner, A. Leonidov and H. Weigert, *Phys. Rev.* **D59**, 014014 (1999), [arXiv:hep-ph/9706377]; *Nucl. Phys.* **B504**, 415 (1997), [arXiv:hep-ph/9701284]; J. Jalilian-Marian, A. Kovner and H. Weigert, *Phys. Rev.* **D59**, 014015 (1999), [arXiv:hep-ph/9709432]; A. Kovner, J. G. Milhano and H. Weigert, *Phys. Rev.* **D62**, 114005 (2000), [arXiv:hep-ph/0004014] ; E. Iancu, A. Leonidov and L. D. McLerran, *Phys. Lett.* **B510**, 133 (2001); [arXiv:hep-ph/0102009]; *Nucl. Phys.* **A692**, 583 (2001), [arXiv:hep-ph/0011241]; E. Ferreiro, E. Iancu, A. Leonidov and L. McLerran, *Nucl. Phys.* **A703**, 489 (2002), [arXiv:hep-ph/0109115]; H. Weigert, *Nucl. Phys.* **A703**, 823 (2002), [arXiv:hep-ph/0004044].

[37] L. V. Gribov, E. M. Levin and M. G. Ryskin, Phys. Rep. **100** (1983) 1.

[38] A. H. Mueller and J. Qiu, Nucl. Phys. **B268** (1986) 427.

[39] A. H. Mueller and B. Patel, Nucl. Phys. **B425** (1994) 471.

[40] J. Bartels, M. Braun and G. P. Vacca, Eur. Phys. J. **C40** (2005) 419 [arXiv:hep-ph/0412218]. J. Bartels and C. Ewerz, JHEP **9909** 026 (1999) [arXiv:hep-ph/9908454]. J. Bartels and M. Wusthoff, Z. Phys. **C6**, (1995) 157. J. Bartels, Z. Phys. **C60** (1993) 471.

[41] M. A. Braun, Phys. Lett. **B632** (2006) 297 [arXiv:hep-ph/0512057]; Eur. Phys. J. **C16** (2000) 337 [arXiv:hep-ph/0001268]; Phys. Lett. **B483** (2000) 115 [arXiv:hep-ph/0003004]; Eur. Phys. J. **C33** (2004) 113 [arXiv:hep-ph/0309293]; **C6**, 321 (1999) [arXiv:hep-ph/9706373]. M. A. Braun and G. P. Vacca, Eur. Phys. J. **C6** (1999) 147 [arXiv:hep-ph/9711486].

[42] Y. V. Kovchegov and E. Levin, Nucl. Phys. B **577** (2000) 221 [hep-ph/9911523].

[43] E. Levin and M. Lublinsky, Nucl. Phys. A **763** (2005) 172 [arXiv:hep-ph/0501173]; Phys. Lett. B **607** (2005) 131 [arXiv:hep-ph/0411121]; Nucl. Phys. A **730** (2004) 191 [arXiv:hep-ph/0308279].

[44] E. Levin, J. Miller and A. Prygarin, Nucl. Phys. **A806** (2008) 245, [arXiv:0706.2944 [hep-ph]].

[45] T. Altinoluk, C. Contreras, A. Kovner, E. Levin, M. Lublinsky and A. Shulkim, Int. J. Mod. Phys. Conf. Ser. **25** (2014) 1460025; T. Altinoluk, N. Armesto, A. Kovner, E. Levin and M. Lublinsky, JHEP **1408** (2014) 007.

[46] T. Altinoluk, A. Kovner, E. Levin and M. Lublinsky, JHEP **1404** (2014) 075 [arXiv:1401.7431 [hep-ph]].; T. Altinoluk, C. Contreras, A. Kovner, E. Levin, M. Lublinsky and A. Shulkin, JHEP **1309** (2013) 115.

[47] E. Levin, JHEP **1311** (2013) 039 [arXiv:1308.5052 [hep-ph]].

[48] A. H. Mueller and B. Patel, Nucl. Phys. **B425** (1994) 471. A. H. Mueller and G. P. Salam, Nucl. Phys. **B475**, (1996) 293. [arXiv:hep-ph/9605302]. G. P. Salam, Nucl. Phys. **B461** (1996) 512; E. Iancu and A. H. Mueller, Nucl. Phys. **A730** (2004) 460 [arXiv:hep-ph/0308315]; 494 [arXiv:hep-ph/0309276].

[49] V. A. Khoze, A. D. Martin, M. G. Ryskin and W. J. Stirling, Phys. Rev. D **70** (2004) 074013 [hep-ph/0406135]; D . N. Triantafyllopoulos, Nucl. Phys. B **648** (2003) 293 [hep-ph/0209121].

[50] M. L. Good and W. D. Walker, Phys. Rev. 120 (1960) 1857.

[51] Y. V. Kovchegov and K. Tuchin, Phys. Rev. D **65** (2002) 074026 doi:10.1103/PhysRevD.65.074026 [hep-ph/0111362].

[52] E. Gotsman, E. Levin and U. Maor, Phys. Rev. D **88** (2013) no.11, 114027, [arXiv:1308.6660 [hep-ph]].

[53] C. W. De Jagier, H. De Vries, and C. De Vries, *Atomic Data and Nuclear Data Tables*, **Vol.14 No. 5,6**, 479 (1974).

[54] E. Gotsman, E. Levin, U. Maor and S. Tapia, Phys. Rev. D **93** (2016) no.7, 074029, [arXiv:1603.02143 [hep-ph]].

[55] Y. M. Shabelski and A. G. Shuvaev, JHEP **1411** (2014) 023, [arXiv:1406.1421 [hep-ph]]; Eur. Phys. J. C **75** (2015) no.9, 438, [arXiv:1504.03499 [hep-ph]]; S. Bondarenko and E. Levin, Eur. Phys. J. C **51** (2007) 65, [hep-ph/0511124]; S. Bondarenko, E. Levin and J. Nyiri, Eur. Phys. J. C **25** (2002) 277, [hep-ph/0204156]; J.J.J. Kokkedee, *" The Quark Model"*, NY, W.A. Benjamin, 1969 and references therein; H. J. Lipkin and F. Scheck, Phys. Rev. Lett. **16** (1966) 71; E. M. Levin and L. L. Frankfurt, JETP Lett. **2** (1965) 65.

[56] E. Iancu, K. Itakura and L. McLerran, Nucl. Phys. A **708** (2002) 327, [hep-ph/0203137]; A. M. Stasto, K. J. Golec-Biernat and J. Kwiecinski, Phys. Rev. Lett. **86** (2001) 596, [hep-ph/0007192]; E. Levin and K. Tuchin, Nucl. Phys. B **573** (2000) 833, [hep-ph/9908317]. Nucl. Phys. B **387** (1992) 617.

[57] E. Levin and A. H. Rezaeian, *"Hadron production at the LHC: Any indication of new phenomena,"* AIP Conf. Proc. **1350** (2011) 243, [arXiv:1011.3591 [hep-ph]]. Phys. Rev. D **82** (2010) 054003, [arXiv:1007.2430 [hep-ph]]; Phys. Rev. D **82** (2010) 014022, [arXiv:1005.0631 [hep-ph]].

[58] Y. L. Dokshitzer, Phil. Trans. Roy. Soc. Lond. A **359** (2001) 309 [hep-ph/0106348].; V. A. Khoze, W. Ochs and J. Wosiek,

"Analytical QCD and multiparticle production," In *Shifman, M. (ed.): At the frontier of particle physics, vol. 2* 1101-1194,2000, [hep-ph/0009298]; Y. L. Dokshitzer, V. A. Khoze and S. I. Troian, J. Phys. G **17** (1991) 1585.

[59] H. Navelet and R. B. Peschanski, Nucl. Phys. **B 507**, 35 (1997) [hep-ph/9703238]; Phys. Rev. Lett. **82** (1999) 1370 [hep-ph/9809474]; Nucl. Phys. B **634** (2002) 291 [hep-ph/0201285].

[60] I. Gradstein and I. Ryzhik, *Table of Integrals, Series, and Products*, Fifth Edition, Academic Press, London, 1994.